Thesis for the Degree of Master of Science

Crystal growth and excited-state dynamics of Eu^{2+} Luminescence in Eu-doped LiBaF$_3$ single crystals

by

Liang SHI

Department of Physics

The Graduate School

Pukyong National University

August   2008

Crystal growth and excited-state dynamics of Eu^{2+} Luminescence in Eu-doped LiBaF$_3$ single crystals

Advisor: Prof. Hyo Jin Seo

by

Liang SHI

A thesis submitted in partial fulfillment of the requirements
for the degree of Master of Science

In Department of Physics, The Graduate School,
Pukyong National University

August 2008

Crystal growth and excited-state dynamics of Eu^{2+}

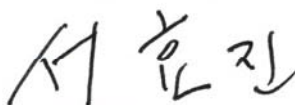Luminescence in Eu-doped $LiBaF_3$ single crystals

A dissertation

by

Liang SHI

Approved as to style and content by:

_____

Prof. Byung Kee Moon

Chair of Committee

_____

Prof. Byeong Eog Jun

Member of Committee

_____

Prof. Hyo Jin Seo

Member of Committee

August, 2008

Contents

Crystal growth and excited-state dynamics of Eu^{2+} luminescence in Eu-doped LiBaF$_3$ single crystals

Liang SHI

Department of Physics
Pukyong National University

Abstract

The pure and europium doped LiBaF$_3$ single crystals were grown by the Czochralski method. The details of the reagent preparation and the crystal growth were investigated. The different concentrations of Eu-doped powder were checked by XRD. The Eu^{2+} ion substitutes for Ba^{2+} ion in the LiBaF$_3$ crystal. The reaction conditions were investigated to get pure LiBaF$_3$ powder. The emission spectra showed the *4f-4f* line emission peak at 359 nm and the *5d-4f* emission band at around 410 nm. The spectra of Eu^{2+}-doped crystals with different concentrates were compared and the concentration quenching was not observed up to the Eu-concentration of 2 mol%. The luminescent lifetime of 359 nm and 410 nm emissions were measured in the temperature range from 15 K to 300 K. The non-exponential decay curves at 410 nm were discussed in relation with the interaction between the excited *4f* and *4f5d* levels. A practical method was introduced to calculate the *4f-5d* activation energy (ΔE) and the value of this energy gap was 950 cm^{-1}. The configurational coordinate model of the LiBaF$_3$: Eu^{2+} was introduced to explain the results. The mechanism of the nonradiative transitions between the excited *4f* and *4f5d* states was discussed.

1. Introduction

1.1 General situation

It is well recognized that the rare earths have the most complicated optical spectra of the elements. This is because the incomplete *4f* shell produces a very large number of low-lying levels and the transitions between them give many-line spectra [1].

One of the most impressive features about the optical spectra of the rare earth ions in different types of host lattices is the sharp lines shown in both the absorption and emission spectra. The rare earth ions can be present in solids either in the divalent or trivalent state in which electronic configurations of them are $4f^n5s^25p^6$ and $4f^{n-1}5s^25p^6$, respectively. Thus, the electrons in the *4f* shell are well shielded by other electronic shells. The transitions within the *4f* configuration are forbidden for the electric dipole transition by the parity selection rule. However, they are usually observed in crystals due to the effects of some special crystal fields which mix some different parity states into the *4f* states. For the trivalent rare earth ions, the $4f^n$ configuration is relatively isolated and the $4f^{n-1}5d$ lies in a high energy above the ground term of the $4f^n$ configuration [1]. For the divalent rare earth ions, the energy separation between the $4f^n$ and $4f^{n-1}5d$ configurations depends on a host lattice and the transitions between them can be observed

in the range of UV to visible.

The spectra of the oxide and fluoride crystals are quite different. Blasse et al. [2] compared the absorption spectra of the $Y_2O_3:Eu^{3+}$ and $YF_3:Eu^{3+}$, which illustrates the influence of the host lattice on the optical absorption of the Eu center. In the fluoride, the spectral positions tend to be at slightly higher energy than those in the oxide and the splitting patterns are different. The first main factor for the different spectral properties of a given ion in different host lattices is covalency. For increasing covalency, the interaction between the electrons is reduced, since they can spread out over wider orbital which is called the electron cloud expanding effect. Consequently, the electron transitions between energy levels with an energy difference which is determined by electron interaction shift to lower energy for increasing covalency. Another factor is the effect of the crystal field which determines the spectral position of a certain optical transition. In addition, the different crystal fields are responsible for the different splitting patterns of certain optical transitions.

Many kinds of the fluoride crystals have been studied during the last few decades such as fluoroperovskites-type (ABF_3, A=Li, Na, K, B=Mg, Zn, Ba), fluorite-type (MeF_2, Me=Ca, Sr, Ba) and halofluoride-type (ABF, A=Ca, Sr Ba, B=Cl, Br) [1]. The substitutes of the rare earth ions in different kinds of the fluoride crystals are obviously different. For example, in $KMgF_3$ and

KZnF$_3$ single crystals, the Eu^{2+} ion substitutes for the singly-charged cation (K$^+$) with a twelvefold fluorine coordination and the charge-compensation defect is located in the second cation coordination sphere giving rise to complex with axial symmetry. However, in LiBaF$_3$, the Eu^{2+} ions possess the doubly-charge Cation (Ba^{2+}) in a twelvefold coordination.

1.2 Properties of the Eu^{2+} ion

The Eu^{2+} ion is the most well-known and widely applied ion with the [Xe]4f^7 structure. Rubio [1] summarized the properties of the Eu^{2+} ion by comparing the absorption and emission spectra in different solids. The absorption spectra of doubly-valent europium ions in solids which consist of two structured broad bands situated in the ultraviolet region. The intensity of the two broad band spectra is quite large as compare to the intra-configurational *f-f* transitions, since the transitions from the ground state to the *4f5d* state (hereafter, the *4f5d* state notes *5d* state) are parity allowed. The emission spectra of the Eu^{2+} ion can be obtained by excitation at either of the two broad absorption bands. Normally, there is only one broad band in the spectrum whose peak position depends strongly on the type of host crystal. The transition of this broad band emission is parity allowed and its decay time is about 1 µs. Its emission color strongly depends on the host lattice by the same factors as in the case of the Ce^{3+} ion [2].
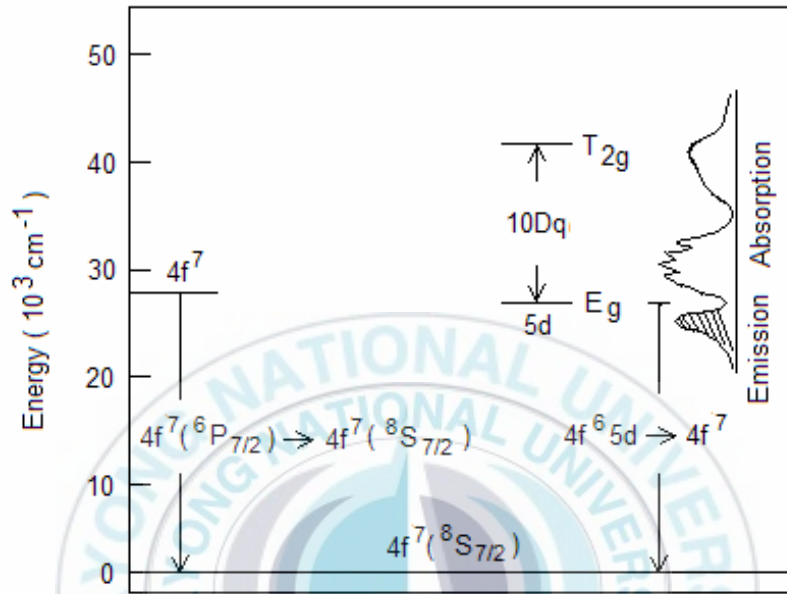
Fig.1.1 Schematic energy level diagram of the Eu^{2+} ion in a crystal. The degeneracy of the *5d* level is split into the doubly-degenerate(E_g) and the threefold-degenerate(T_{2g}) energy levels. 10 Dq is the energy gap between the T_{2g} and E_g levels.

If the influence of the crystal field and the covalence are weak, the lowest component of the *5d* configuration lies in such a position that the energy is higher than the excited *4f* (hereafter, the excited *4f* state is called *4f'* state) configuration. At low temperature, it's possible that the excited Eu ions relax to the *4f'* level. Although *4f'*—*4f* transition is parity forbidden, sharp-line emission spectra due to the $^6P_{7/2} \rightarrow {}^8S_{7/2}$ also can be observed

4

[3, 4]. According to the ligand field theory, the degeneracy of the *5d* level can be split into doubly-degenerate(E_g) and threefold-degenerate(T_{2g}) energy levels, which is due to the effect of crystal field acting on the Eu^{2+} site. The separation between them is the well-recognized 10 Dq splitting. For eightfold and twelvefold coordination of the ligands, the E_g level is situated at a lower energy compared with the T_{2g} level. However, in sixfold and fourfold coordination the situation is reversed. Figure 1.1 is the schematic energy level diagram of the Eu^{2+} ion in a crystalline solid where the relation with the *4f* and *5d* levels can be observed clearly [1].

1.3 An introduction of LiBaF$_3$

Crystalline LiBaF$_3$ is a typical ABF$_3$ material (herein A-alkali ion, B-alkali-earth ion, X-halide ion) which has inverse-perovskite with cubic structure (a_0 = 3.988 Å) [5]. The Li$^+$ ion is surrounded by six F$^-$ ions while the Ba^{2+} ion by twelve F$^-$ ions. The regular lattice site of Ba^{2+} ion in LiBaF$_3$ has the O_h point group symmetry [6] and the crystal cell of the LiBaF$_3$ is shown in figure 1.2. When Eu^{3+} (EuF$_3$ used) ion is incorporated in the LiBaF$_3$ lattice, on a regular site, it must be accompanied by a charge compensating defect. Actually, when Eu^{3+} ion enters the lattice, F$^-$ ion will be oxidized to compensate the charge. The chemical equation is shown as follows [7],

$$Eu^{3+} + F^- \Leftrightarrow Eu^{2+} + F$$
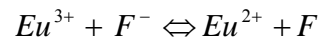
The ionic radius of Eu^{2+} (1.17 Å) is closer to the Ba^{2+} radius (1.35 Å) than that of Eu^{3+} (0.95 Å). The valence of Eu^{2+} ion is the same as that of Ba^{2+} ion. Thus, the structure of Eu^{2+} substituting the Ba^{2+} site is more stable than that of Eu^{3+}.This is the reason why the EuF_3 is used and finally the Eu^{2+} ion is the main component substituting the Ba^{2+} ion in $LiBaF_3$ crystals. However, the complete reaction of the Eu^{3+} and F^- ion is impossible which indicates the existence of Eu^{3+} ion.

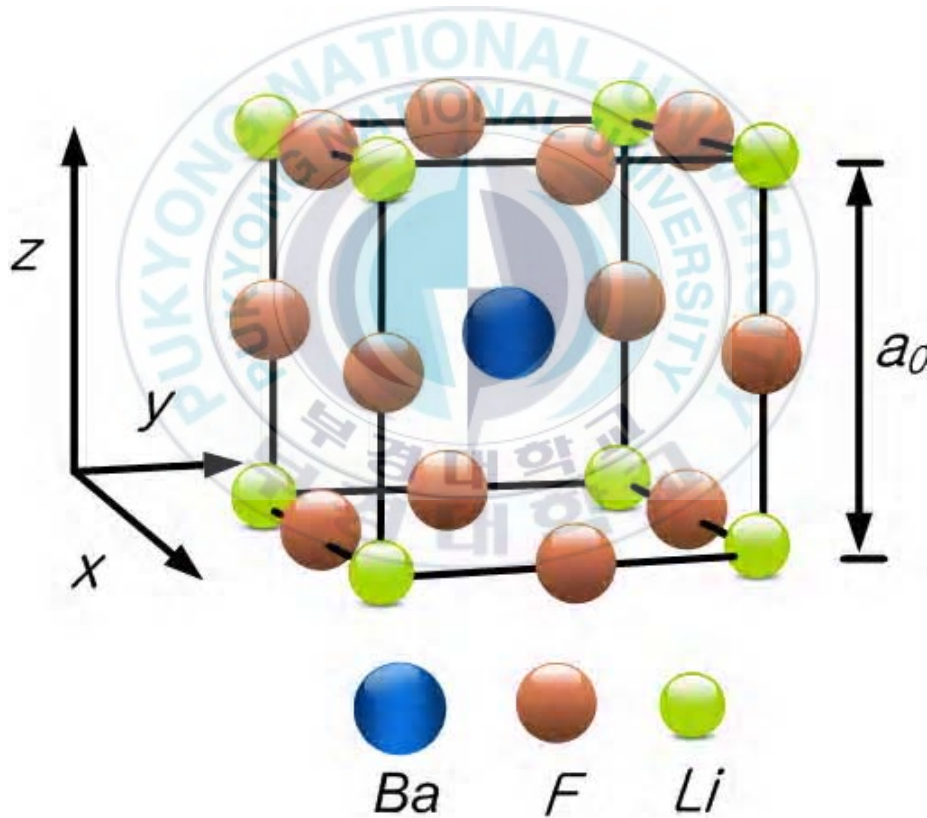Fig.1.2 The structure of pure $LiBaF_3$ crystalline is cubic. The Li^+ ion is surrounded by six F^- ions while the Ba^{2+} ion by twelve F^- ions. The doped Eu^{2+} ion substitutes the Ba^{2+} ion in it.

In the past thirty years much research has been concentrated on the properties of rare earth ions doped $LiBaF_3$ material. In 1972, Leckebusch et al. [8] firstly reported the Co^{2+}, Eu^{3+}, Sm^{3+} and Nd^{3+} ions doped $LiBaF_3$ crystals which were grown by the Czochralski and Bridgman methods. Baldochi et al. [5] introduced a temperature program and an interface shape which could influence the optical homogeneity and optical transmission. In another literature he also discussed the different crystallographic orientation and rotation rate which influence the optical and crystalline quality [9]. Bensalah et al. [10] measured the IR absorption spectrum and thermal expansion coefficient of the $LiBaF_3$ single crystal. Tyagi et al. [11] tested the thermo-stimulated luminescence of Eu^{3+} doped $LiBaF_3$. Gektin et al. [12] showed the color center emission spectra in his article.

Many kinds of methods were used to synthesize $LiBaF_3$. Bensalah et al. [10] used the Czochralski method. Meijerink et al. [13] used Bridgman method. Fujihara et al. [14] used pyrolytic synthesis method. Shi et al. [15] also introduced a solvothermal process method. It is reported that several kinds of ions have been doped into the $LiBaF_3$ such as Pb^{2+}, Ce^{3+}, Mg^{2+}, Eu^{2+}, Yb^{2+} and Eu^{3+} [5, 11, 12, 16, 17, 18]. Having good luminescence and optical properties, pure and doped $LiBaF_3$ have been investigated in many kinds of practical application. Gektin et al. [19] reported it as a scintillation detectors and dosimetry material. Xia et al. [17] reported it as an X-ray storage material.

1.4 Experimental objective

Meijerink reported a very classic literature about $LiBaF_3:Eu^{2+}$ [20]. He made a comparison between the two isoelectronic ions Eu^{2+} and Gd^{3+}. The magnetic dipole transition probabilities of the $^8S_{7/2} \rightarrow {}^6P_{7/2}$ and $^8S_{7/2} \rightarrow {}^6P_{5/2}$ transitions for Eu^{2+} were determined and compared to values of Gd^{3+}. Also, he compared the vibronic coupling strengths of intra-$4f^7$ transitions with Eu^{2+} and Gd^{3+}. The temperature dependent ratio of the anti-Stokes and Stokes vibrations was measured.

Although Meijerink reported such a good literature in which many theoretic problems had been investigated in detail, we decide to learn the $LiBaF_3:Eu^{2+}$ from some new viewpoints. The $LiBaF_3:Eu^{2+}$ sample that Meijerink used was powder which was synthesized by solid state reaction. It is known that the spectroscopic property of single crystal is better than that of powder. This author did not give the XRD diagram to certify the powder was single phase. Temperature dependent decay of the $^8S_{7/2} \rightarrow {}^6P_{7/2}$ transition in $LiBaF_3:Eu^{2+}$ was investigated. However, the lifetime of the transition from the *4f5d* to the ground state was not reported. The energy level scheme of Eu^{2+} in the $LiBaF_3$ was not given in that literature and the activation energy was not calculated accurately.

Considering the experimental feasibility and existing apparatus in our lab, we decided to concentrate our minds on the Czochralski method and dope the europium ion in $LiBaF_3$ crystals. The main purpose of this experiment is using the emission spectra and decays to draw the configuration coordinate of Eu^{2+} ion and discuss the mechanism of the interaction between the excite *4f* and *5d* levels in Eu^{2+} doped $LiBaF_3$ single crystals.

In our experiments, we grew four different concentrate (0, 0.1, 0.5, 2 mol%) $LiBaF_3$ crystals which were checked by XRD. In the present work, we have measured the emission spectra and lifetime of the Eu^{2+} ions in the $LiBaF_3$ lattice from low temperature to room temperature. We observed a broad band emission with a maximum at 410 nm and a line emission with a peak at 359 nm which are corresponding to *5d-4f* and *4f'-4f* transitions, respectively. The lifetime of the parity allowed *d-f* transition is much shorter than that of the parity forbidden *f'-f* transition. We calculated the activation energy (ΔE) from the temperature dependent decay which was measured from 17 K to room temperature.

2. Theory and analysis

2.1 Crystal growth by the Czochralski method and phase diagram analysis

The Czochralski method is named after Polish scientist Jan Czochralski, who discovered this method in 1916 while investigating the crystallization rates of metal. It's a particular method of crystal growth, wherein a seed is touched on top of the melt contained in a crucible and drawn slowly at a controlled rate. Then the crystal grows below the seed. The seed and the crystal are often rotated to provide a uniform growth environment. The rate of rotation and pulling speed can be changed to get single crystals with different diameters. Fluid motion within the melt is important because it affects the quality of the crystal. The flow driving forces considered are buoyancy, crystal rotation and surface-tension gradient.

Before growing the crystal, we have to synthesize $LiBaF_3$ powder by using solid state reaction. Leckebusch et al. [8] showed the phase diagram of the LiF-BaF_2 system in figure 2.1. From this diagram, we find that $LiBaF_3$ melts incongruently and its single crystal must be grown from a non stoichiometric melt to avoid other phase precipitation. At high temperature, LiF powder is easy to volatilize. Thus, we confirm that the approximate ratio
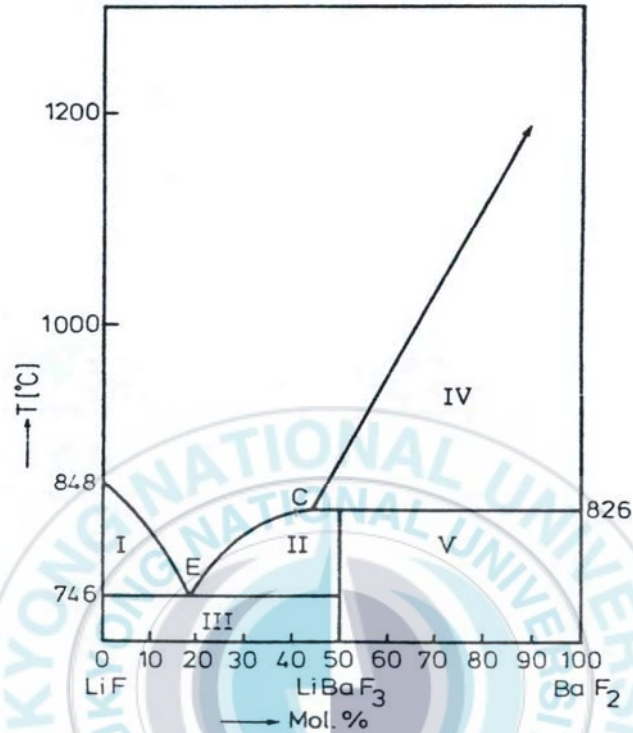
Fig.2.1 Phase diagram of the LiF-BaF$_2$ system [8]. Ⅰ.LiF(S) +LiBaF$_3$(L). Ⅱ.LiBaF$_3$(S+L). Ⅲ.LiF(S)+LiBaF$_3$(S). Ⅳ.BaF$_2$(S)+LiBaF$_3$(L). Ⅴ.LiBaF$_3$(S)+BaF$_2$(S). CE is the Two-phase Curve (Melting Curve).

of the LiF:BaF$_2$ is 3:2 and the possible melting point of the LiBaF$_3$ is near 790 ℃. In order to get pure LiBaF$_3$ powder and be convenient to dope Eu ions into it, we select 650 ℃ as the solid reaction temperature.

2.2 Radiative and nonradiative transitions [2]

When a luminescence material absorbs energy from the surrounding and arrives in a high energy excited state, how does it return to the ground state and release the additional energy? In general, there are two ways to return to the ground state, radiative and nonradiative processes. Figure 2.2 shows the configurational coordinate diagram. There are many cases that will be discussed as follows,

(1). Consider the parabola g and e. In this diagram, they are the same shape, but parabola e is the excited state of the ground state (g). There is no offset between g and e, and they will never cross. When the luminescent ion absorbs energy and goes to the lowest vibrational level of the excited state (e), this ion can spontaneously emit energy to return to the ground state and this sharp emission line is called zero-phonon line. If the energy is a little high, this ion is excited to the high vibrational level, the excited ion has to relax the additional energy to the lowest vibrational level and return to the ground state. This relaxation process is one of the nonradiative ways.

(2). Consider an electron is excited to anther orbit such as the *4f-5d* absorption of the Eu^{2+} ion. Also, the electron can be excited from the ground state (g) to the edge of the excited state (e') in this figure. There is an offset (ΔR) between the parabolas of the ground (g) and excited (e') state. Then the excited
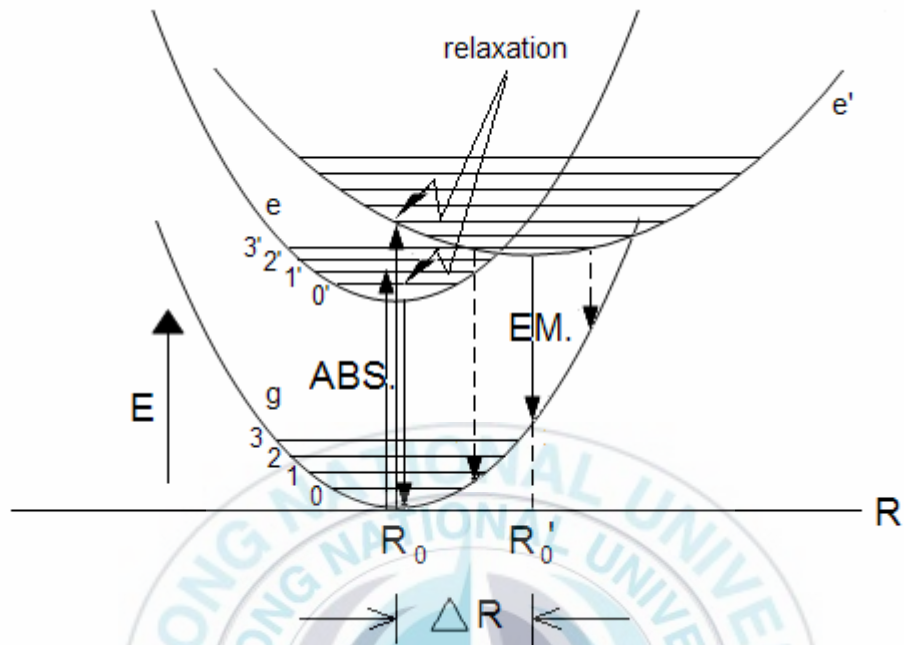
Fig. 2.2 Configurational coordinate diagram. E is radiative energy. ABS. is the absorption process. Em. is the emission process. Parabola e is the excited state of the ground state g. e' is the excited state of another level.

ion relaxes its additional energy and returns to the lowest vibrational level where the transition of the e' to g state occurs a broad band spectrum.

(3). If the temperature is high enough, the electron via the cross of e' and g state, it is possible to return to the ground state in a nonradiative way. The excited energy is then completely given up to heat the lattice.

(4). Consider a transition from the parabola e to e'. The parallel parabolas (e and g) generally belong to the same configuration, so that they are

considered to be a forbidden optical transition. But transition from e' to g is normally allowed. Absorption occurs from the ground state to e'. Also, the nonradiative transition between e and e' is possible. Now, the emission occurs from e state, which is a line emission.

2.3 Calculation of lifetime and activation energy (ΔE)

2.3.1 Calculation of lifetime

Lifetime is a very important property of the excited state. For allowed emission transitions it is short, for forbidden transition it is long. For a two-level system the population of the excited state decreases according to [2]

$$\frac{dN_e}{dt} = -N_e P_{eg} \qquad (2\text{-}3\text{-}1)$$

Where N_e is the number of luminescent ions in the excited state after an excitation pulse, t is the time, and P_{eg} is the probability for spontaneous emission from the excited state to the ground state.

Integration yields,

$$N_e(t) = N_e(0)e^{-P_{eg}t} \qquad (2\text{-}3\text{-}2)$$

Equation (2-3-2) is also written as

$$N_e(t) = N_e(0)e^{-t/\tau_R} \tag{2-3-3}$$

Where τ_R is the radiative decay time. Natural logarithm of the equation (2-3-3) is

$$\ln\frac{N_e(t)}{N_e(0)} = -t/\tau_R \tag{2-3-4}$$

Thus,

$$\tau_R = -\frac{t}{\ln[N_e(t)/N_e(0)]} \tag{2-3-5}$$

2.3.2 Calculation of the *4f-5d* activation energy

The luminescence spectrum of $LiBaF_3$:Eu^{2+} consists of *4f'-4f* line emission and *5d-4f* band emission. The occurrence of line emission indicates that in $LiBaF_3$:Eu^{2+} the lowest excited *4f* level lies below the lowest *5d* level. The energy difference between these two levels is called the *4f-5d* activation energy (ΔE).

A method was reported to calculate this energy [3]. It can be derived from the temperature dependence of the line and band luminescent intensity ratio(R) of the $LiBaF_3$:Eu^{2+} single crystal. If it is assumed that the lowest excited *4f* level is populated via the lowest *5d* level, *R* can be written as follows,
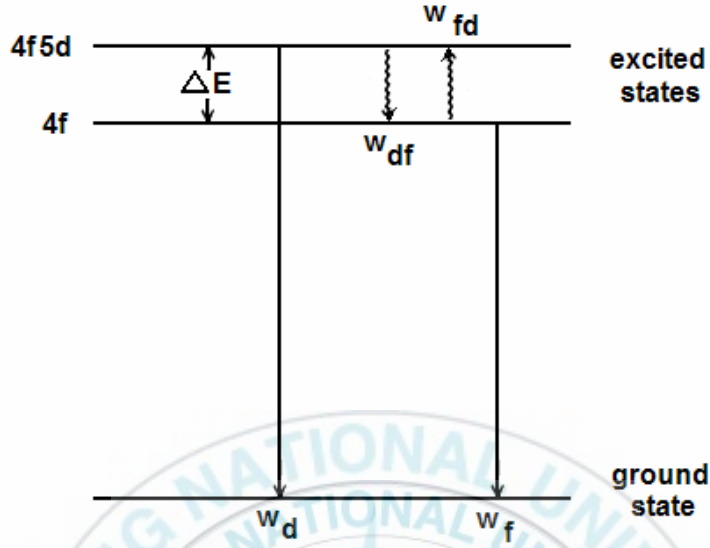
Fig. 2.3 Energy level scheme for excited *4f* and *5d* emissions. Where g_d, g_f and W_d, W_f are the degeneracies and radiative probabilities of the lowest *5d* level and the lowest excited *4f* level, respectively. W_{df} is the probability of the transition from the lowest *5d* level to the lowest *4f'* level. W_{fd} is the probability of the transition from the lowest *4f'* level to the lowest *5d* level. Wavy arrows and straight arrows indicate the nonradiative and radiative transitions, respectively.

$$R = \frac{(g_f / g_d)(w_f / w_d)\exp(\Delta E / kT)}{1 + (g_f / g_d)(w_f / w_{df})\exp(\Delta E / kT)} \qquad (2\text{-}3\text{-}6)$$

Where g_d, g_f and w_d, w_f are the degeneracies and radiative probabilities of the lowest *5d* level and of the lowest excited *4f* level, respectively. w_{df} is the probability of the transition from the lowest *5d* level to the lowest excited *4f* level. Using the approximation $g_d = g_f$ [3], equation (2-3-6) can be written as

16

$$R = \frac{(w_f / w_d) \exp(\Delta E / kT)}{1 + (w_f / w_{df}) \exp(\Delta E / kT)} \qquad (2\text{-}3\text{-}7)$$

At low temperature, the LiBaF$_3$:Eu^{2+} crystal mainly emits line emission, viz. $w_d < w_{df}$. Since the *4f'-4f* transition is parity forbidden and the *5d-4f* is parity allowed, the radiative probability $w_f \ll w_d$, also that $w_f \ll w_{df}$. If the temperature is not too low, the second term in the denominator of eq. (2.3.7) can be negligible. Therefore, the eq. (2-3-7) can be described by

$$R \cong (w_f / w_d) \exp(\Delta E / kT) \qquad (2\text{-}3\text{-}8)$$

Logarithm of the eq. (2-3-8)

$$\log R = \log(w_f / w_d) + \log[\exp(\Delta E / kT)]$$
$$= \log(w_f / w_d) + \frac{\ln[\exp(\Delta E / kT)]}{\ln 10}$$
$$= \frac{\Delta E}{kT \ln 10} + \log(w_f / w_d) \qquad (2\text{-}3\text{-}9)$$

Eq. (2-3-9) can be written as

$$\log R = \frac{\Delta E}{(10^3 \times \ln 10)k}(10^3 T^{-1}) + \log(w_f / w_d) \qquad (2\text{-}3\text{-}10)$$

After measuring the *4f'* line and *5d* band emission spectra from low temperature to room temperature, we can get a series of temperature dependent ratio (R) from the integrated intensity of the line emission and that of the band emission. The value of the R also can be defined as

$$R = \frac{\int I(T)_{line}\, dT}{\int I(T)_{band}\, dT} \tag{2-3-11}$$

An approximate line can be set in the coordinate diagram for log R as Y-axis and $10^3 T^{-1}$ as X-axis. ΔE can be derived from the slope of the line. Consider the result of the equation (2-3-10), the value of the slope is

$$Slope = \frac{\log R}{10^3 T^{-1}} = \frac{\Delta E}{(10^3 \times \ln 10)k} \tag{2-3-12}$$

Finally, the value of the activation energy can be written as

$$\Delta E = Slope \times (10^3 \times \ln 10)k \tag{2-3-13}$$

3. Sample preparation and spectroscopic measurements

3.1 Growth procedure of the LiBaF$_3$ single crystal

The pure and Eu-doped LiBaF$_3$ powders were prepared by solid state reaction method at high temperature. Determination of the melting point and the rate of raising temperature were carried out by DTA (PERKIN-ELMER, DTA 7e). Lattice parameters and phase identification were measured by XRD (PHILIPS, X'Pert-MPD System). The crystals were grown in the platinum crucible which was laid in the chamber filled with high purity Argon gas. The all grown crystals were cut to standard samples (3×4×5 mm).

3.1.1 Synthesis procedure of LiBaF$_3$ powder

The mole ratio of LiF (99.9%): BaF$_2$ (99%) was confirmed 3:2, and the concentrations of the doped EuF$_3$ were 0.1, 0.5, 2 mol%, respectively. The admixture was placed in a reagent bottle. Then, the reagent bottle was laid on a ball miller in order to mix the powder completely. 10 hours later, the mixed powder was obtained and measured by DTA to analysis the melting point. From figure 3.1, the melting point is known near 790 ℃.

Then, the powder was loaded into a platinum crucible which would be

covered by a ceramic cover. The crucible was laid in the center of the chamber and encased with some small aluminium balls. Finally, the chamber was sealed and pumped to get a vacuum atmosphere. The powder must be dried at 300 ℃ for about 10~20 hours in the chamber and the vacuum pump was always opened in this step. After drying, the powder was heated up to 650 ℃ at a speed of 2 ℃/min. Since the solid state reaction process needed 10 hours at 650 ℃, the vacuum pump was also turned on in this process. Finally, we grinded the compound and repeated those steps again to get better reactant.
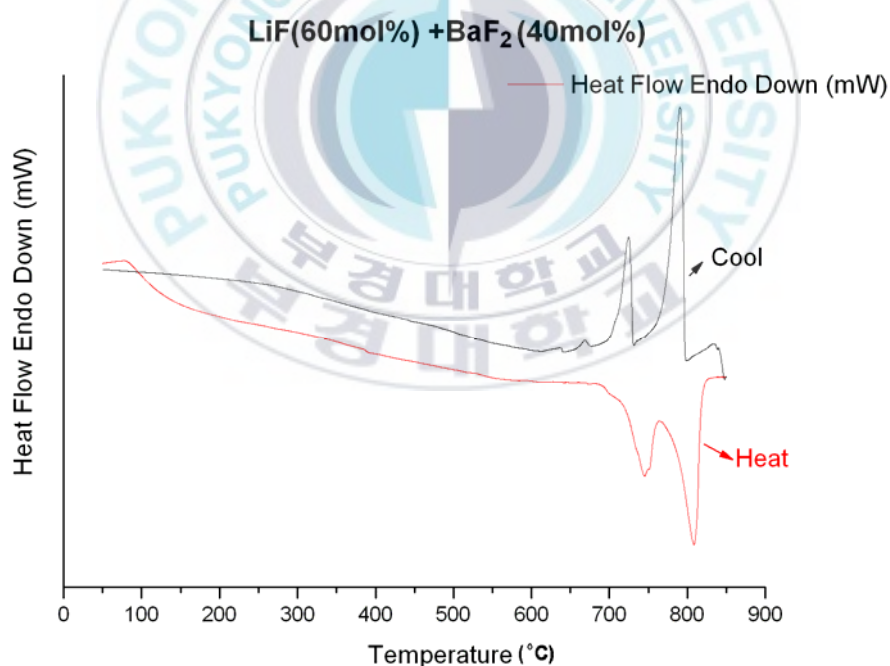

Fig. 3.1. Differential thermo-gravimetric analysis (DTA) of LiF-BaF$_2$ system. In the heating curve, there are two absorption peaks, and the stronger one is the melting-point-peak.

3.1.2 X-ray diffraction (XRD) analysis

Determination of the lattice parameters and phase identification of sample were carried out by the X-ray powder diffraction method. The data was collected by a scanning mode with a step of 0.02 degree in the 2θ range from 20 to 90 degrees. The result is shown in the figure 3.2. The lattice parameters a, b, c are the same value (3.995 Å), which shows the structure of the sample is cubic. Also, the result agrees well with value of the JCPDS 18-0715 card, which means the sample is pure $LiBaF_3$ powder with the space group Pm3m.

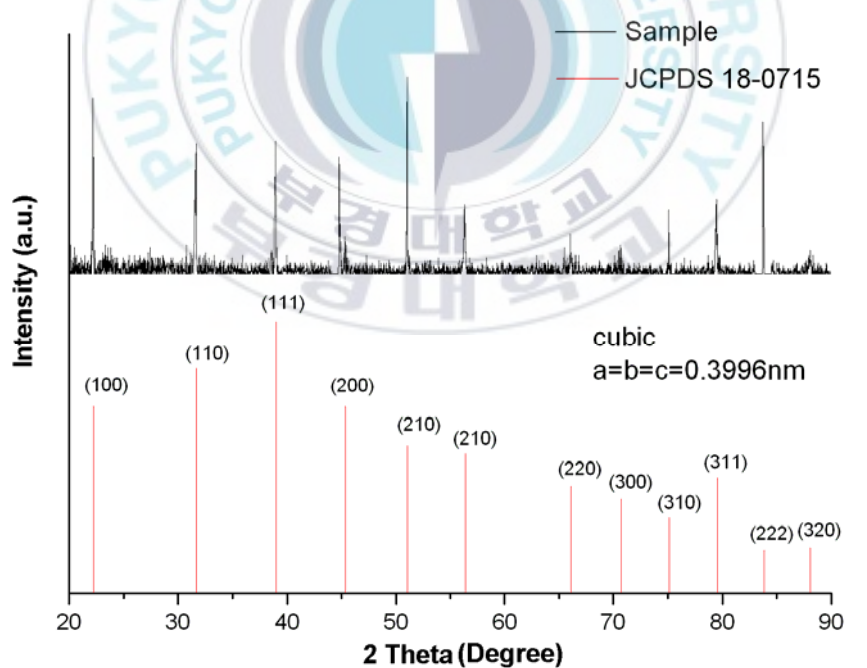Fig. 3.2 XRD diagram of the $LiBaF_3$ powder. This data matches the JCPDS 18-0715 card very well.

3.1.3 Crystal growth of LiBaF$_3$ single crystals

The Czochralski method began with pure or Eu-doped LiBaF$_3$ powder which was prepared by solid state reaction method. The apparatus of the Czochralski method is shown in the figure 3.3. A lot of pure powder was placed in a large platinum crucible. Then, the crucible was put in a steel chamber and encased with some aluminum balls. Next, the chamber was closed and the pump was turned on to get a vacuum atmosphere. When the powder was heated to 300 ℃, the chamber was filled with argon gas (1～1.5 kgf/cm^2) and the gas was pumped out for 3 times to get a pure argon gas atmosphere. The powder was heated up to a set temperature which is 20 or 30 ℃ lower than melting point, then we increased the temperature to the melting point slowly (1～2 ℃/min) by changing heating program control to manual control.
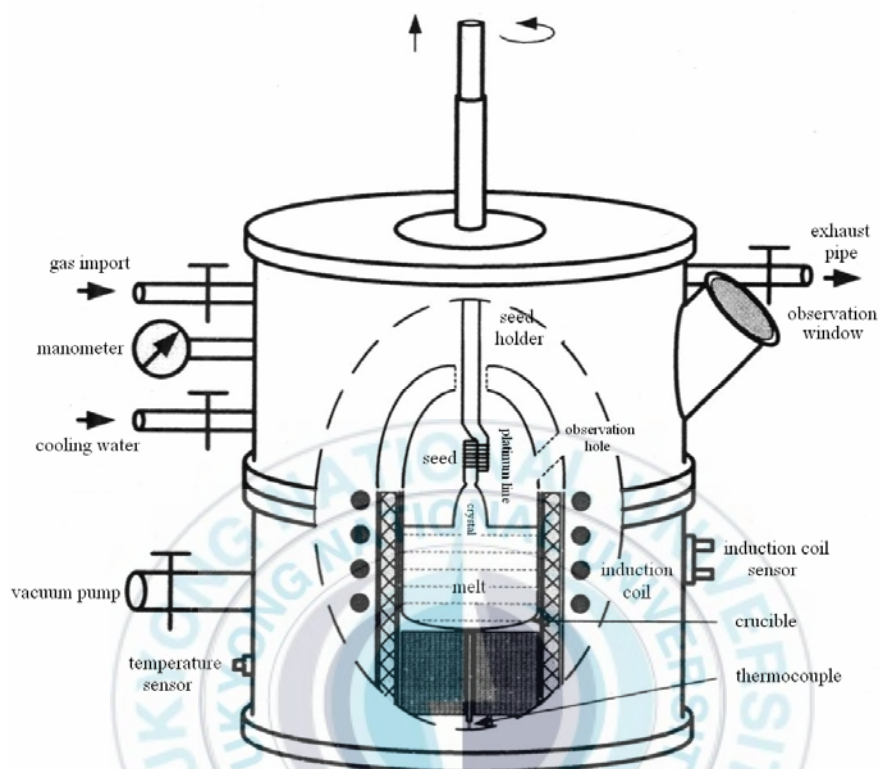
Fig. 3.3 Illustration of crystal growth chamber. Pure $LiBaF_3$ crystal seeds were used to grow single crystals.

When the powder was melted, a small seed crystal mounted on the end of a rotating shaft was slowly lowered until it just dipped the surface of the red-hot melt. Then, the rotating rod was drawn upwards with a speed (1 mm/h). In this process, we can adjust temperature, rotation speed and pulling speed to change shape of crystal. The crystal can be grown from two to four centimeters or long, depending on how much powder there is in the crucible. At the end of growth process, we slowly increased the pulling speed to a high value (3 mm/h or high) to separate the crystal from hot melt.

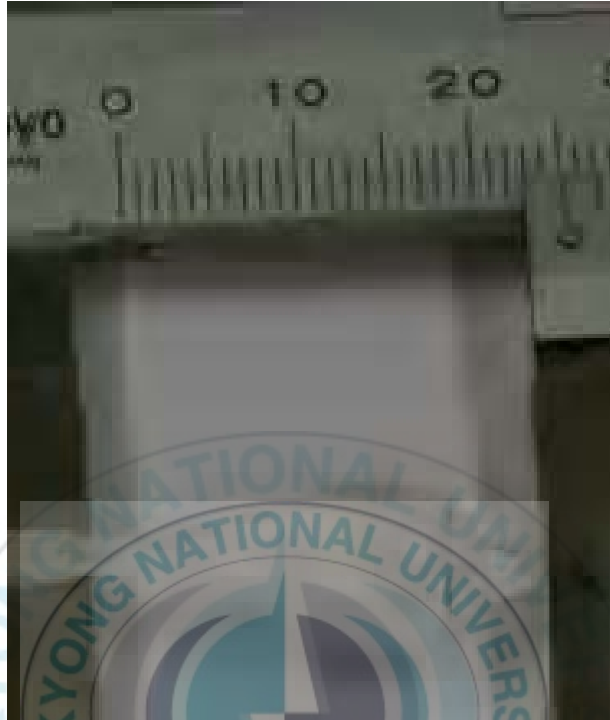Fig. 3.4 LiBaF$_3$ single crystal. Though there are some cracks at the bottom of this crystal, it is transparent and the size is enough to cut.

Then, keep the crystal at a position which is 0.5~1 cm higher than the melt for 2 h to get symmetrical temperature gradient . Finally, the crystal was slowly cooled to room temperature at the speed of 1 ℃/min. One of the crystals grown by the Czochralski method is shown in figure 3.4.

3.1.4 Sample machining

We grew LiBaF$_3$ single crystals with four different concentrate (0, 0.1, 0.5, 2 mol%). Although there are some small cracks inside the crystal, it is transparent and the size is enough to cut. In fact, we can choose the center part of it to test. The crystals were cut to standard samples (3×4×5 mm). Then we polished it to get good optic performance. The total preparation procedures of the sample are shown in figure 3.5.

Weighing (LiF 60mol%, BaF$_2$ 40mol%, EuF$_3$)
⬇
Mixing and Grinding (5h)
⬇
Differential Thermo-gravimetric Analysis (DTA)
⬇
Drying (120 °C, 10h) and Calcination (650 °C, 10 h)
⬇
X-Ray Diffraction Analysis
⬇
Crystal growth (1mm/h, 30rpm, Argon atmosphere)
⬇
Cutting (3 × 4 × 5mm) and Polishing
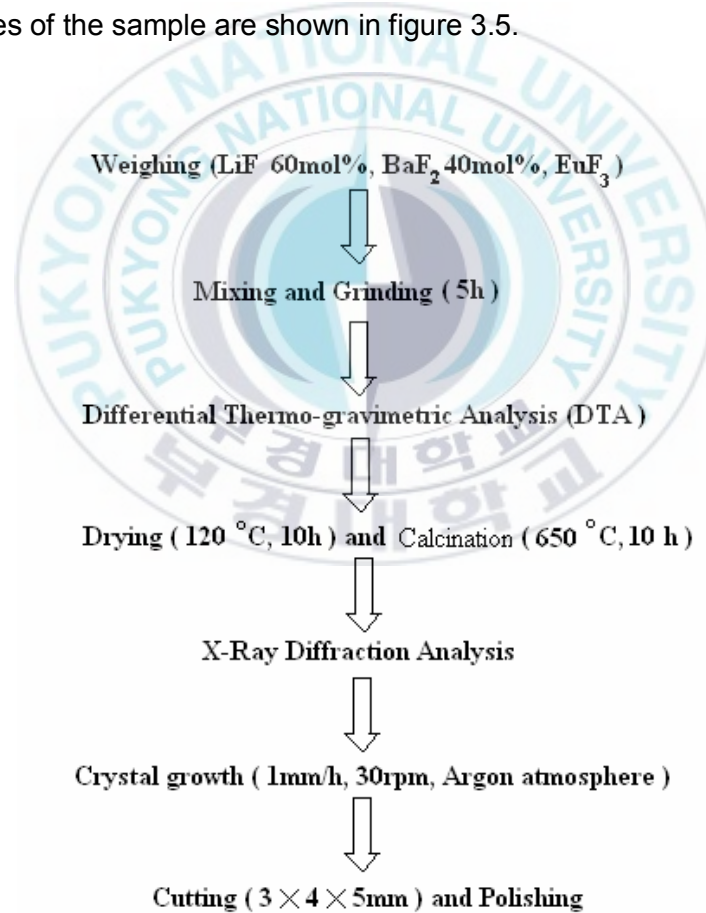
Fig. 3.5 Preparative procedures diagram of the LiBaF$_3$ single crystal.

3.2 Spectroscopic measurements

The spectroscopic measurements of $LiBaF_3:Eu^{2+}$ single crystals were preformed by the pulsed Nd: YAG laser at 266 nm (Spectron Laser System SL802G). The samples were attached to a holder which was placed in a helium gas flow cryostat in a variable temperature region (10-300 K). The 266 nm laser beam with 25 mJ pulse energy was focused and crossed the polished faces. The emission spectra were measured by monitoring the emission intensity in different wavelengths under the pulsed laser excitation. The lifetimes were measured for the excited $LiBaF_3:Eu^{2+}$ samples. The luminescence was dispersed by the 75 cm monochromator (Acton Research Corp. Pro-750) and multiplied by the PMT (Hamamatsu R928). The slit width of the monochromator was regulated to get suitable emission spectra. The data was displayed and recorded with the LeCloy 9301 digital storage oscilloscope. The equipment diagram of this spectroscopy system is showed in figure 3.6 [21].
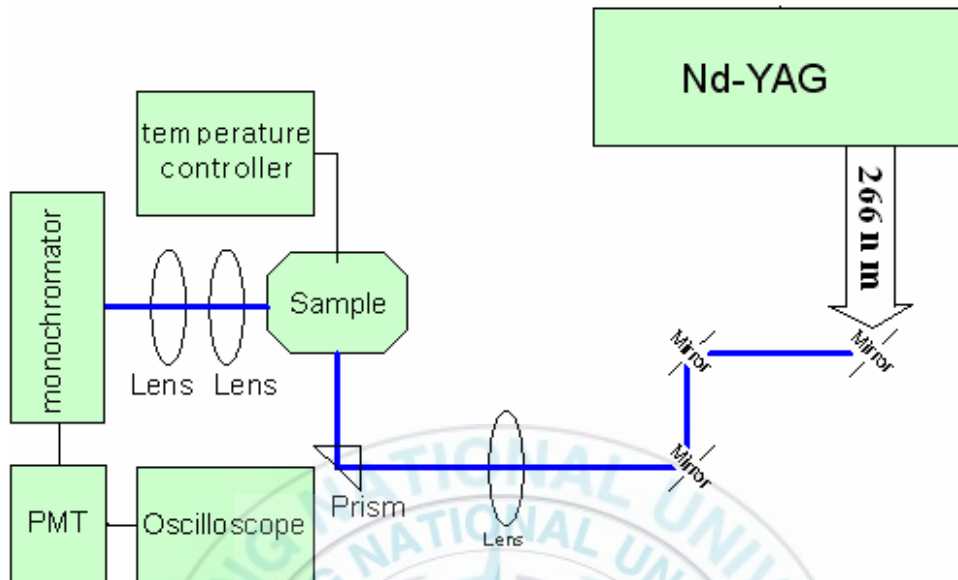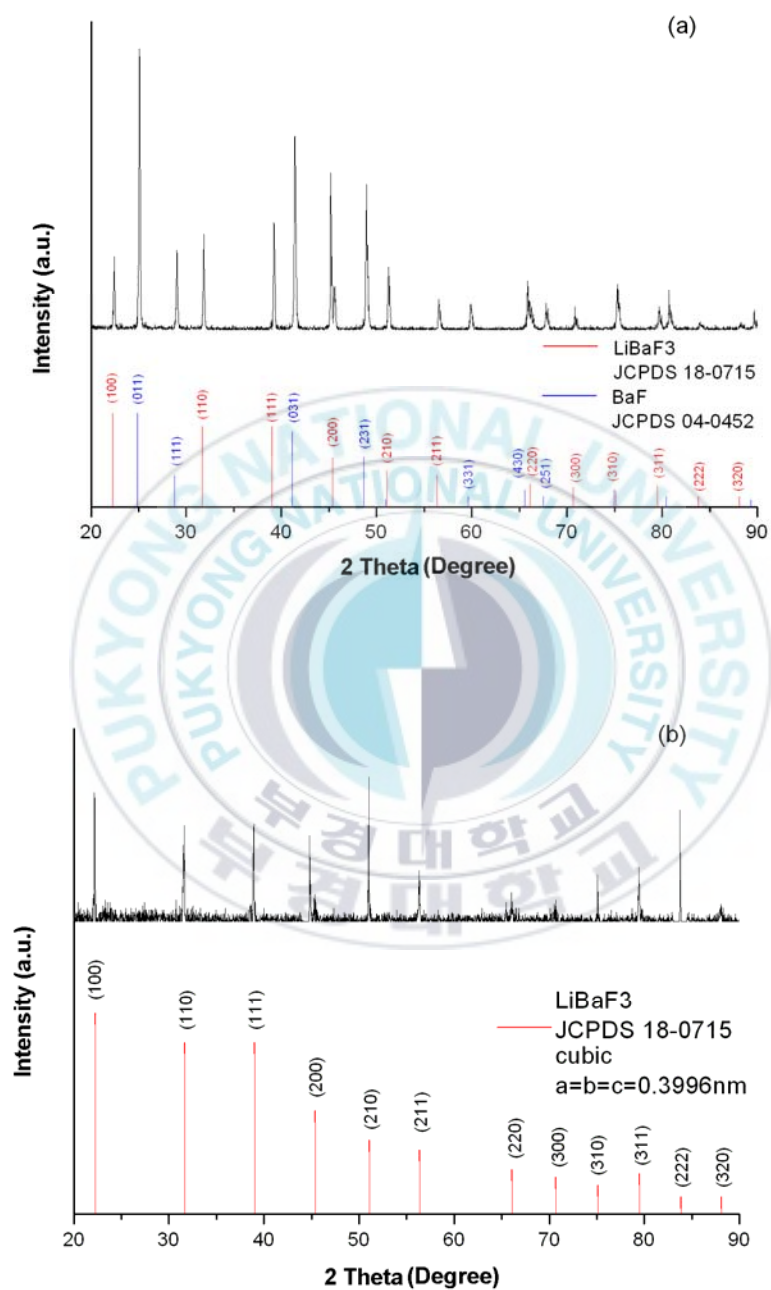
Fig. 3.6 The equipment diagram of spectroscopy measurement system. The Nd:YAG laser was pumped to get a beam of 266 nm laser which was transmitted to the workbench by a group of mirror. The 266 nm laser with 25 mJ energy was focused by a lens and crossed two polished faces of the LiBaF$_3$:Eu^{2+} single crystal which was cooled by a helium gas flow cryostat.

4. Results and discussion

4.1 Two factors of the powder preparative procedures

4.1.1 Different degrees of calcination

Before discussing the influence of calcination degree to the powder, we prepared two samples. The Li/Ba ratio and weight of them are the same. The calcination temperature of them we set was 650 ℃. The XRD diagrams of the calcined powders are shown in fig. 4.1 (a) and fig. 4.1(b). Sample (a) was calcined one time and sample (b) was done two times. We can see the differences of these two figures clearly. Because of the uncompleted solid state reaction, there are two phases in sample (a). One phase is $LiBaF_3$ (JCPDS 18-0715 card) with the lattice parameter a=0.3996 nm, and another is BaF_2 (JCPDS 04-0452 card) which is possible to increase defects in the crystal. Since the diffraction intensity of BaF_2 is very strong, the concentration is very high in fig. 4.1(a). The peaks in fig. 4.1(b) are in good agreement with the JCPDS 18-0715 card. Thus, we can conclude that the different degree of calcination is a very important factor for the raw material.

(a)

Intensity (a.u.)

LiBaF3
JCPDS 18-0715
BaF
JCPDS 04-0452

(100)
(011)
(110)
(111)
(031)
(111)
(200)
(231)
(210)
(211)
(331)
(430)
(220)
(251)
(300)
(310)
(311)
(222)
(320)

2 Theta (Degree)

(b)

Intensity (a.u.)

LiBaF3
JCPDS 18-0715
cubic
a=b=c=0.3996nm

(100)
(110)
(111)
(200)
(210)
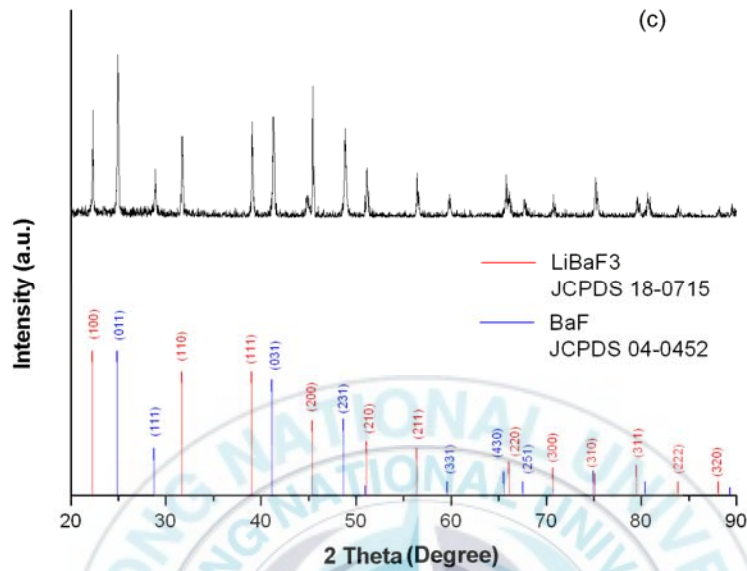(211)
(220)
(300)
(310)
(311)
(222)
(320)

2 Theta (Degree)

29

Fig.4.1 XRD diagrams of the LiBaF$_3$ powder. (a) LiF 60 mol% after one time calcination, (b) LiF 60 mol% after two times calcination, (c) LiF 55 mol% after two times calcination.

4.1.2 Different ratio of the LiF and BaF$_2$ powders

In order to compare the effect of the concentration of LiF and BaF$_2$ raw materials, we prepared another compound that the mole ratio of LiF/BaF$_2$ was 55:45. The XRD diagram is shown in figure 4.1 (c). Also, it was calcined two times and the component of BaF$_2$ can be found. For the volatility of the LiF and the incongruently meltability of LiBaF$_3$, the non-stoichiometric compound was prepared to avoid other phases in LiBaF$_3$ melt. However, it is very hard to match the mole ratio of these raw materials. According to the

phase diagram of LiF-BaF$_2$ system, we can confirm a possible ratio to do the experiment. In this case, we need to prepare different concentration mixture. Comparing the figure 4.1 (b) and (c), we found that 60 mol% of LiF is better than 55 mol% one.

4.2 Several factors of the crystal growth

4.2.1 The initial temperature cooling rate

Firstly, we grew the crystal with <001> seed and a constant rotation 30 rpm. The initial temperature cooling rate was -1 ℃/h. The diameter of growing crystal grew gradually reaching a final constant value of 16 mm. The length of it was about 15 mm. The temperature was kept for 10 hours to get an equal-diameter crystal. Then, we changed the temperature rate to -1.5 ℃/h. 5 hours later we finished the process with -2 ℃/h to separate the crystal from the melt.

Because the initial rate of temperature cooling rate was a little fast, the neck of the crystal was very short and wide. The increase of the weight resulted in the appearance of the cracks which affect the crystalline homogeneity and optical transmission.

We also began the crystal growth with a lower temperature rate in the

same condition. In this case (-0.5 ℃/h), a better diameter control was obtained. The final constant value was 10 mm with 12 mm length. The shape of the neck was better than before. The most important was the decrease of the defects.

Considering the thermal condition of the chamber and the dimensions of the crucible, we have to increase the diameter of the crystal in order to get a bigger crystal, which needs a faster temperature cooling rate. As a result, more defects appeared.

4.2.2 Rotation and pulling speed

Different rotation speeds result in different interface shapes of the growing crystal. For the $LiBaF_3$ single crystal used of the Czochralski method, the solid interface becomes concave towards the melt for high rotation rate, flat for middle rate and convex for low rotation rate [5]. We can get a bigger crystal by changing the rotation speed. For different points at the face of the melt, the temperatures are different. Using faster speed might cause asymmetry of the temperature which results in more defects inside the growing crystal. But the crystal is very difficult to grow at low rotation speed. After repeating many times, we found 30-40 rpm is a best choose.

Pulling speed is also a very important factor for crystal growth by the

Czochralski method. The difference of the temperature from button to top of the crucible is very big without platinum attemperator. Thus, the pulling speed we used is lower than 1 mm/h. Otherwise, the optic properties of the crystal is not good.

4.3 The emission spectra of LiBaF$_3$:Eu^{2+} crystals

Time-resolved (200 µs) emission spectra of the different concentration Eu^{2+}-doped single crystals at 17 K are shown in the figure 4.2 (a). Figure 4.2 (b) is the emission spectra at room temperature. As can be seen, a group of line emission peaks at around 359 nm and a broad emission band at around 410 nm are observed. With the same experimental conditions, we can compare the emission intensity of these different concentration samples. We conclude that the concentration quenching is not observes in these samples. The higher Eu^{2+}-concentration gives rise to the stronger peak.
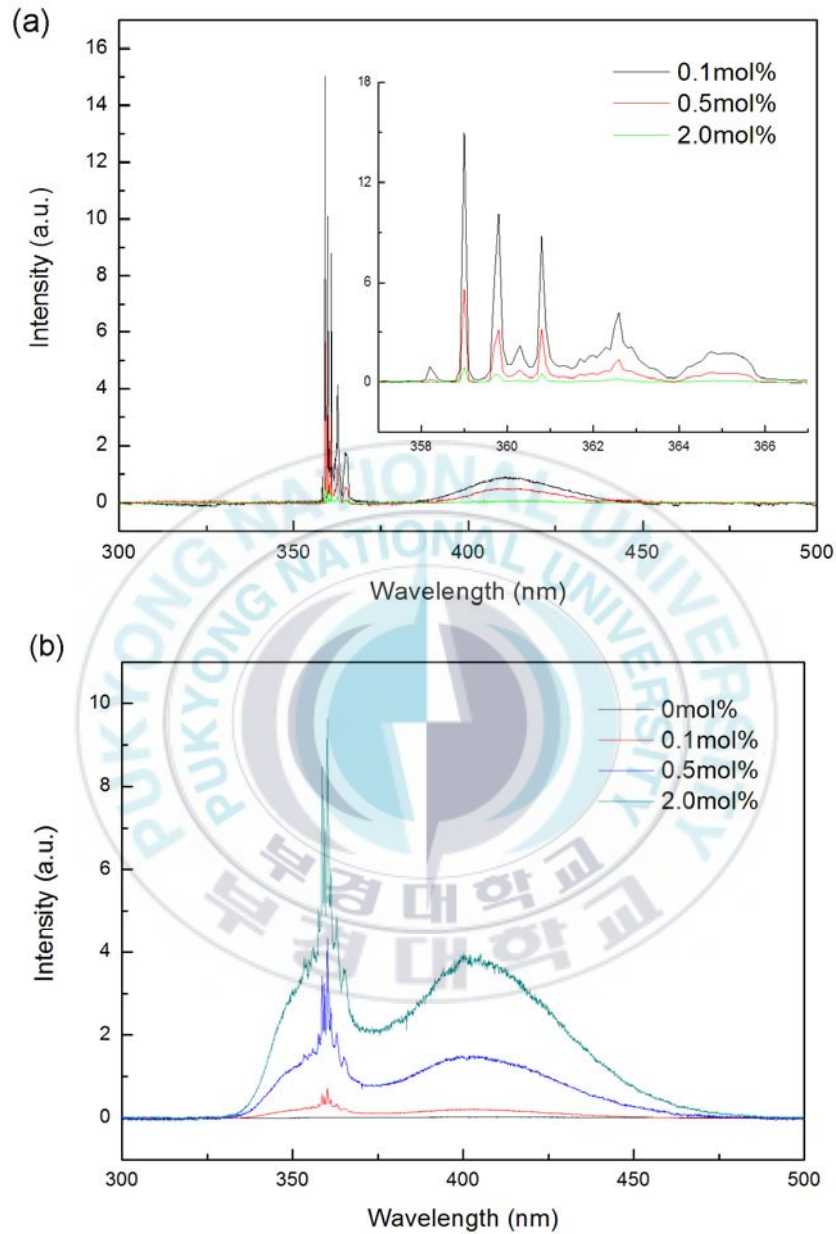
Fig. 4.2 Time-resolved (200 μs) emission spectra of different concentration LiBaF$_3$:Eu^{2+} crystals at 266 nm laser excitation. (a). Emission spectra at 17 K. (b). Emission spectra at 300 K. Line emissions peaking at 359 nm are due to the *4f'-4f* transitions. The broad band emissions are due to the *5d-4f* transitions.

The *4f-4f* transition is a parity forbidden transition, and the *4f* orbit is well shielded by the *5d* orbit. Thus, the emission from the *f-f* transition shows a line emission and the position of this emission in different host lattices is nearly the same. The zero-phonon line at 359 nm is due to the $^6P_{7/2} \rightarrow {}^8S_{7/2}$ transition of Eu^{2+} ion shown in the figure 4.3. The other lines at around 359 nm were reported to be the Stokes and anti-Stokes vibrations [20]. The anti-Stokes and Stokes vibrations are situated at high and low energy sides of the zero-phonon line shown in table 4.1, respectively.
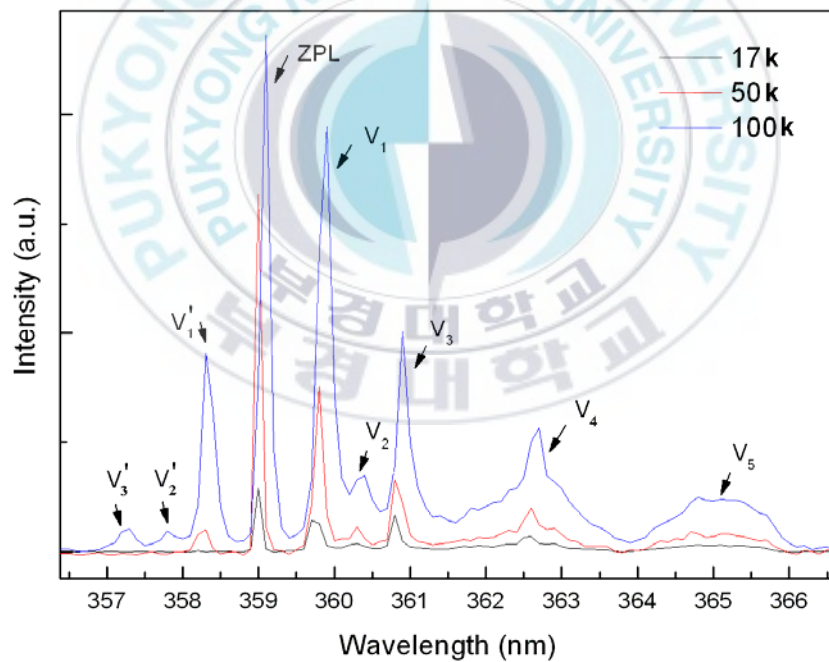

Fig. 4.3 Line emission spectra of the LiBaF$_3$: Eu^{2+} (2 mol%) single crystal at low temperatures. The zero-phonon line (ZPL) was observed at 359 nm. The other peaks were due to Stokes and anti-Stokes vibrations.

At very low temperature, it is not easy to observe the anti-Stokes vibrations. Above the 100 K, they appear at the high energy sides of the zero-phonon line due to the stronger thermal vibration. The peaks at high temperature have a small offset from the 17 K. The intensity of the zero-phonon line and its vibrations are stronger than that at the low temperature.

Table 4.1. The positions of the Stokes and anti-Stokes vibrations at around zero-phonon line (359 nm).

Temperature (K)	Zero-phonon line (nm)	Stokes vib. (nm)	Anti-stokes vib. (nm)
17	359	$v_1 = 359.7$ $v_2 = 360.3$ $v_3 = 360.8$ $v_4 = 362.6$ $v_5 = 364.9$	$v_1^{'} = 358.2$
100	359.1	$v_1 = 359.9$ $v_2 = 360.4$ $v_3 = 360.9$ $v_4 = 362.7$ $v_5 = 365.1$	$v_1^{'} = 358.3$ $v_2^{'} = 357.8$ $v_3^{'} = 357.3$
200	359.2	$v_1 = 360.0$ $v_3 = 361.1$ $v_4 = 362.8$ $v_5 = 365.2$	$v_1^{'} = 358.5$ $v_3^{'} = 357.4$ $v_4^{'} = 355.8$
300	359.4	$v_1 = 360.2$ $v_3 = 361.2$ $v_4 = 362.9$ $v_5 = 365.3$	$v_1^{'} = 358.6$ $v_3^{'} = 357.5$ $v_4^{'} = 356.0$

The *5d-4f* transition is a parity allowed transition. Therefore, the emission spectrum of this transition is a board band and the lifetime is very short. In different host lattices, the position of this emission spectrum is different, which is ascribed to the different crystal field strength on the Eu^{2+} ion. Normally, the intensity of this emission decreases with raising temperature. The time-resolved emission spectra (2 μs) of the *5d-4f* transition in the $LiBaF_3$:Eu^{2+} (2 mol%) single crystal at low temperature are shown in figure 4.4.
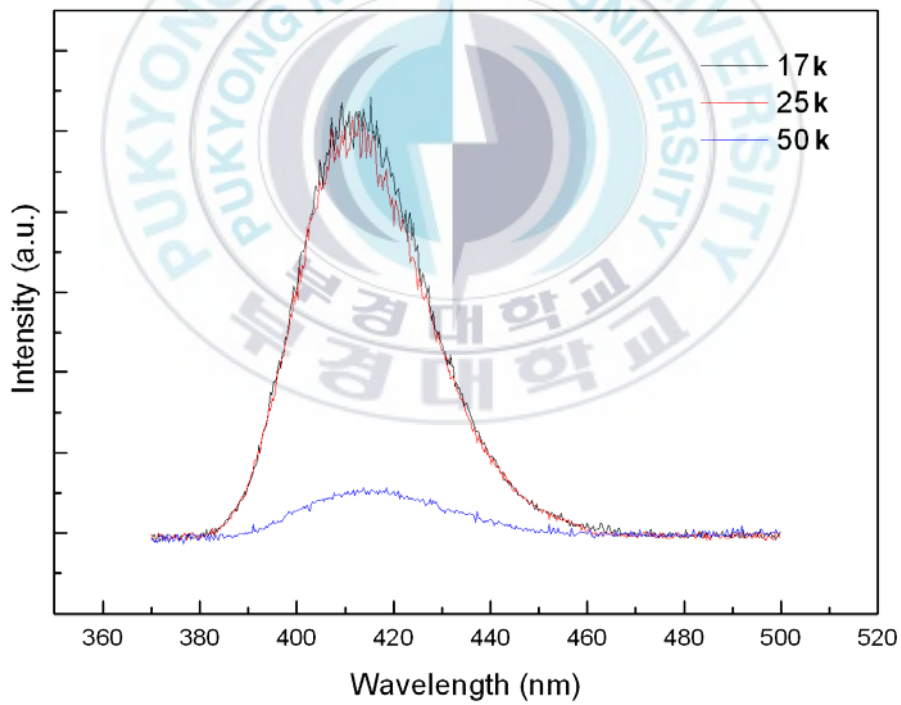

Fig. 4.4. Time-resolved (2 μs) emission spectra of the $LiBaF_3$:Eu^{2+} (2 mol%) single crystal at low temperatures which are due to the *5d-4f* transitions.

4.4 Lifetime and interaction between the excited *4f* and *5d* state

4.4.1 Temperature dependent lifetime of the Eu^{2+}-emission.

The Nd: YAG laser at 266 nm is used to be the excitation source and the Eu^{2+} ion in the LiBaF$_3$ (2 mol%) single crystal can be excited to a high energy level directly. Then, the excited Eu^{2+} ions relax to the lowest level of the *5d* state. A broad band emission occurs and the excited Eu^{2+} ion returns to the bottom of the ground state. However, there is another way back to the *4f* ground state. The excited Eu^{2+} ions relax to the cross point of the excited *4f* and *5d* state along the *5d* curve. The process is shown in figure 4.5 (1).

It is possible that the excited Eu^{2+} ions continue to relax to the lowest vibration level of the excited *4f* state from this point shown in figure 4.5 (2). This nonradiative process has been discussed in the Chapter 2. Thus, the line emission from the *4f'* state to the ground state occurs. Because of the small energy difference of the *d-f'* levels and thermal vibration, the excited ion may not choose to emit the energy at the *4f'* state and has a probability to go back to the *5d* state shown in figure 4.5 (3). It goes along the *4f'* curve and comes to the lowest vibration level of the *5d* state. Then, this excited ion emits the energy and returns to the ground state.
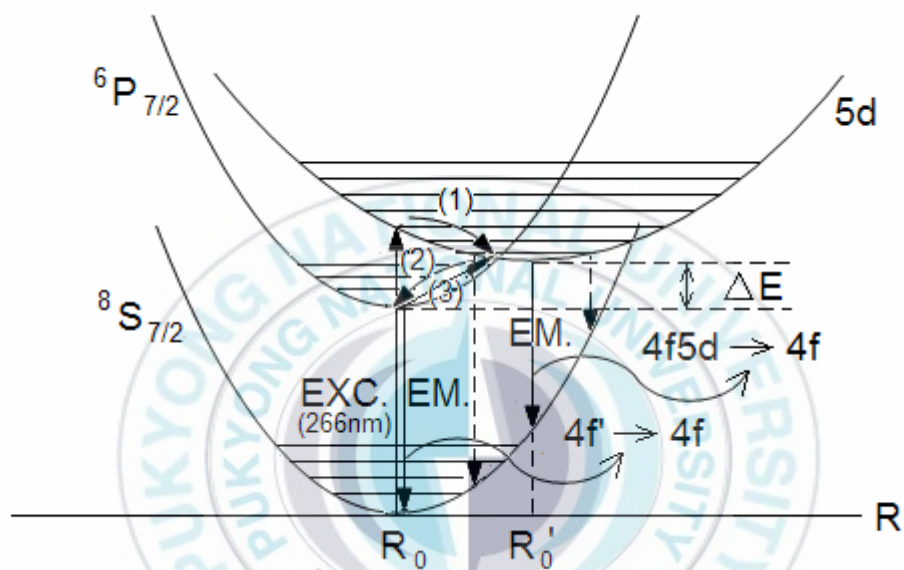
Fig. 4.5 The kinetic model of the Eu^{2+} ion in the $LiBaF_3$ single crystal. Process (1), (2), (3) are the non-radiative transitions. EXC. is the excitation process. Em. is the emission process. ΔE is the energy difference between the excited *4f* and *5d* levels.
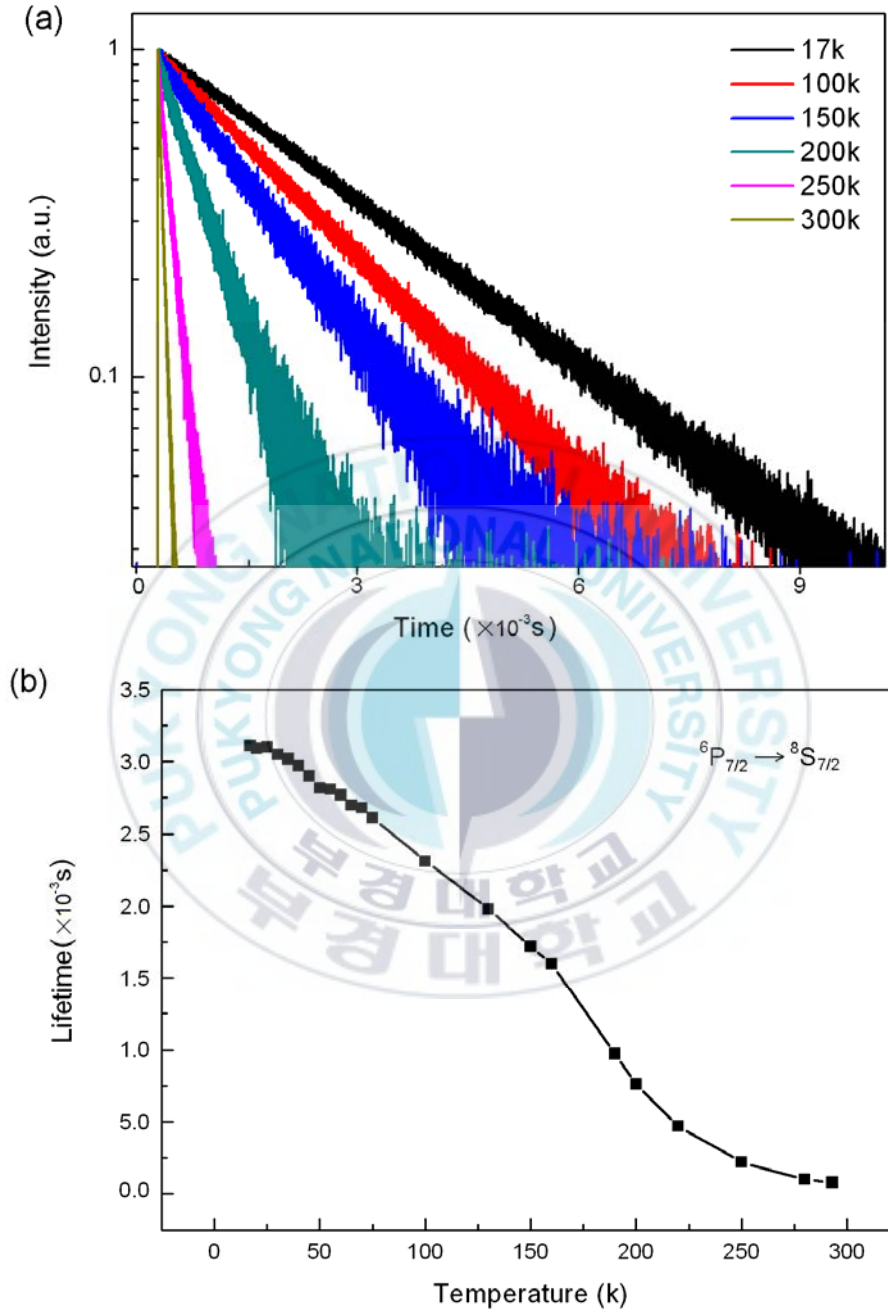
Fig. 4.6 (a) The luminescent lifetimes of the $^6P_{7/2} \rightarrow {}^8S_{7/2}$ transitions from 17 K to 300 K at 359nm. (b) The values of these lifetimes were obtained by 266 nm Nd:YAG laser.

The *5d-4f* emission of the Eu^{2+} ion is parity allowed emission while the *4f'-4f* is parity forbidden. In general, the lifetime of them are short and long, respectively. The temperature dependent lifetimes of the $LiBaF_3:Eu^{2+}$ (2 mol%) single crystal at 359 nm and 410 nm were measured. The decay curves of the $^6P_{7/2} \rightarrow {}^8S_{7/2}$ transition at different temperatures show a series of single-exponential lines which are shown fig. 4.6 (a). In the fig. 4.6 (b), the values of lifetime decrease smoothly from 17 K to 300 K.

The *5d-4f* luminescent lifetimes at 410 nm and the values of them are shown in the figure 4.7. From the fig. 4.7 (a), the decay curves of the $LiBaF_3:Eu^{2+}$ (2 mol%) single crystal are non-exponential and the values are very long. Actually, this kind of decay curve includes two components and the initial part of it is single-exponential. The initial part is very short which is hardly observed at high temperature. The values of the long component lifetime are shown in fig. 4.7 (b), which also decreases smoothly from 17 K to 300 K. In comparison with the values of the 4*f'-4f* transition in fig. 4.6 (b) and the long decay values of the *5d-4f* transition in fig. 4.7 (b), at high temperature ($>$150 K), the lifetime of the *5d* level is nearly the same with the *4f'* level. At 300 K, the lifetime of these two levels are all 70 µs.
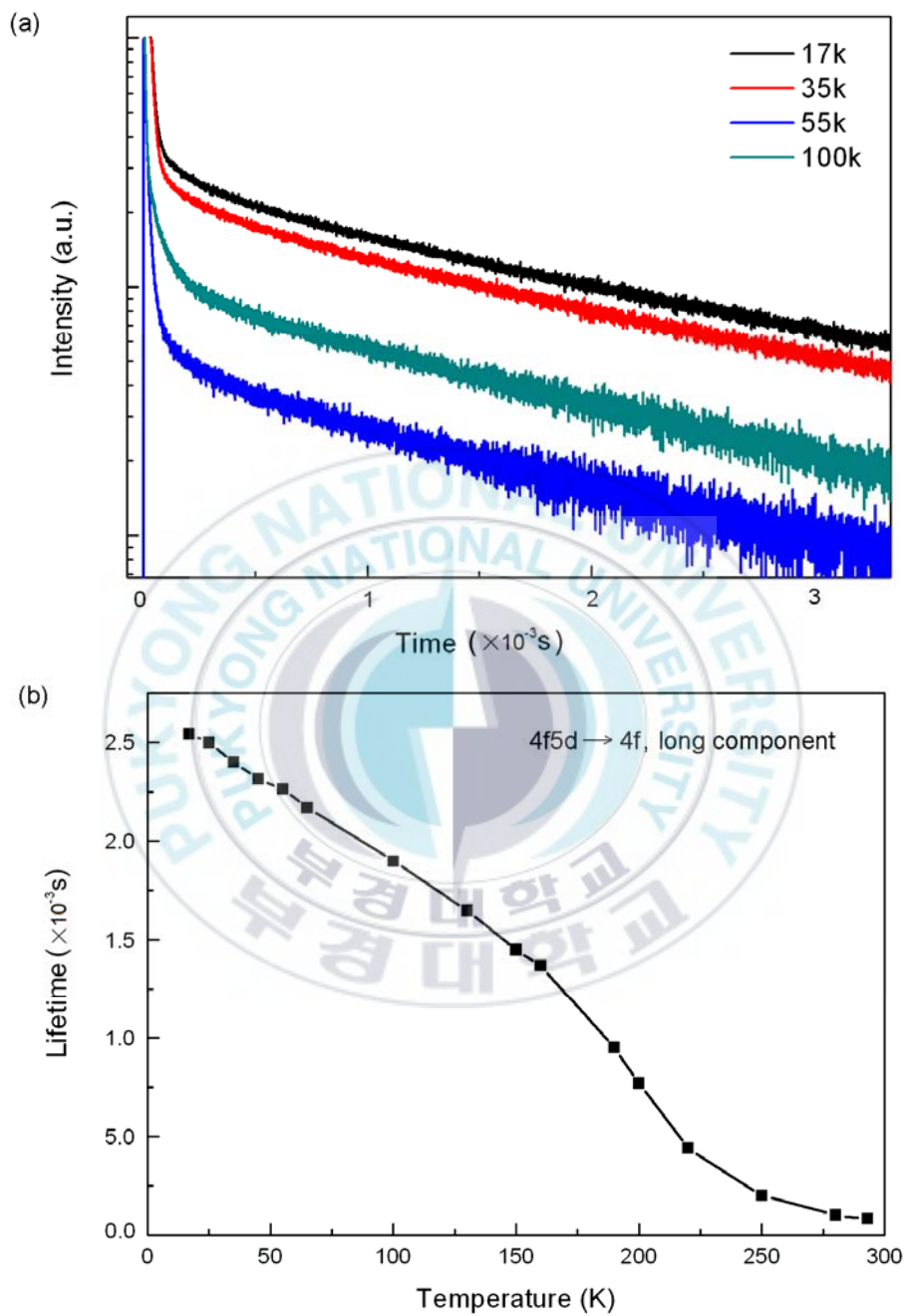
41

Fig. 4.7 The *5d→4f* luminescent lifetimes of the LiBaF$_3$:Eu^{2+} at 410 nm. (a). Full temperature dependent decay curves. (b). The values of long component lifetime.

42

Let's consider the initial part of the figure 4.7 (a) which is independently shown in the fig. 4.8 (a). The lifetime of this part is 700 ns at 17 K shown in fig. 4.8 (b). But it decreases rapidly to 10 ns at 75 K while the long decay part becomes dominating component. Thus, the lifetime of the *5d* level is thought to consist of two kinds of component, one is the normal *5d* short lifetime and another is the long lifetime transferred from the excited *4f* level. As shown in the figure 4.5, the excited Eu^{2+} ion can return to the lowest vibration level of the excited *4f* state. Because of the small energy difference of the *5d-4f'* levels and thermal vibration, the excited ion may not choose to emit the energy at the excited *4f* state and has a probability to go back to the *5d* state shown in figure 4.5 (3). It goes along the excited *4f* curve and comes to the lowest vibration level of the *5d* state. Then, the excited ion emits the energy and returns to the ground state. This back-transfer process results in a decrease of transition probability from the excited *4f* state to the ground state and increases the lifetime of the *5d* state.
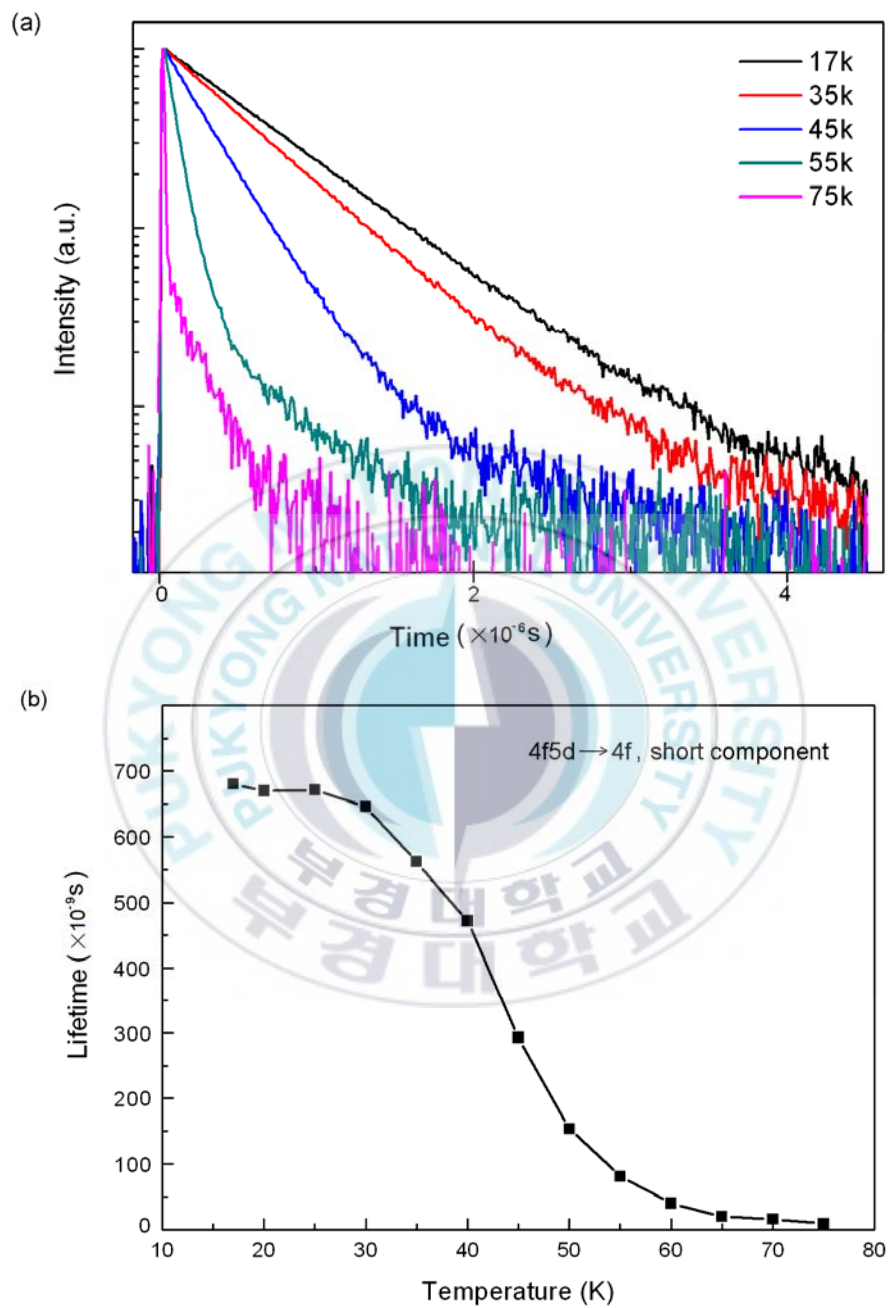
Fig. 4.8 The *5d→4f* luminescent lifetimes of LiBaF$_3$:Eu^{2+} at 410 nm. (a). The initial part of full temperature dependent decay curves. (b). The values of the short component lifetime.

44

Figure 4.9 shows the lifetimes of the *4f'* state and the long component of the *5d* state at low temperature, which indicates an interaction between the excited *4f* and *5d* level. From this figure, we can find that the long component lifetime of the *5d* level has the same trend with the lifetime of the excited *4f* level. Thus, it gives an evidence of the interaction between these two levels.
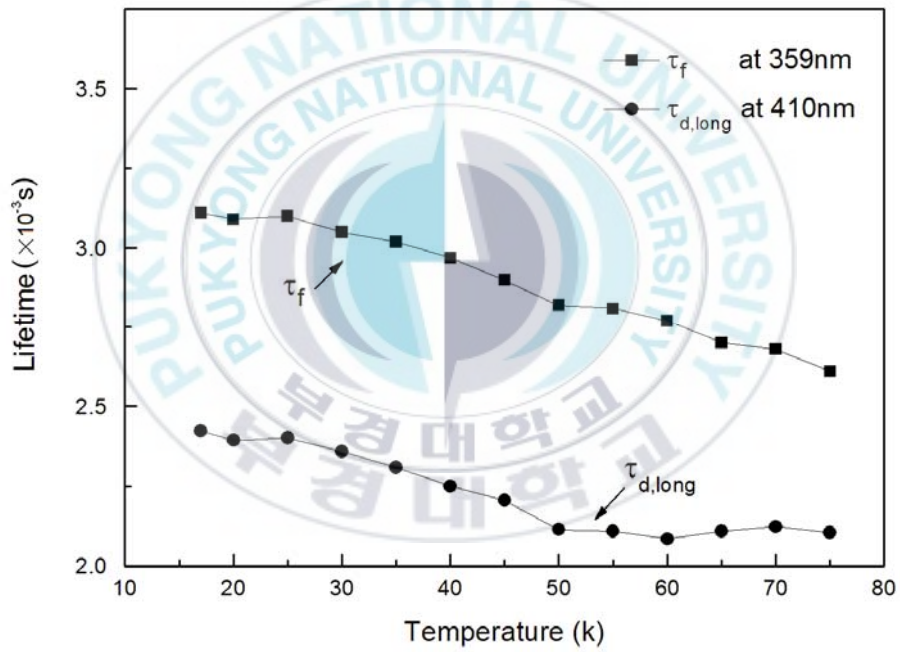

Fig.4.9 The relation between the *4f'* and *5d* long component levels. τ_f is the lifetime of the excited *4f* level at 359 nm, and $\tau_{d,long}$ is the long component lifetime of the *5d* level at 410 nm.

4.4.2 The calculation of the activation energy (ΔE) and the configurational coordinate model

A practical method for calculating the *4f-5d* activation energy (ΔE) has been introduced in the Chap. 2. The temperature dependent lifetimes of the excited *4f* and *5d* levels in the LiBaF$_3$:Eu^{2+} (2 mol%) single crystal also have been measured. For not too low temperatures, the second term in the denominator of the equation (2-3-7) in the Chap. 2 can be negligible. In this case, ratio (R) exponentially depends on temperature. For low temperature, however, the second term is no longer negligible, which results in a flattening of the log R versus 10^3T^{-1} curve in figure 4.10. However, our hypothesis is in not too low temperature. The date points in not low temperature have been fitted to a line, and the value of slope is 0.59582. Thus, the activation energy (ΔE) is

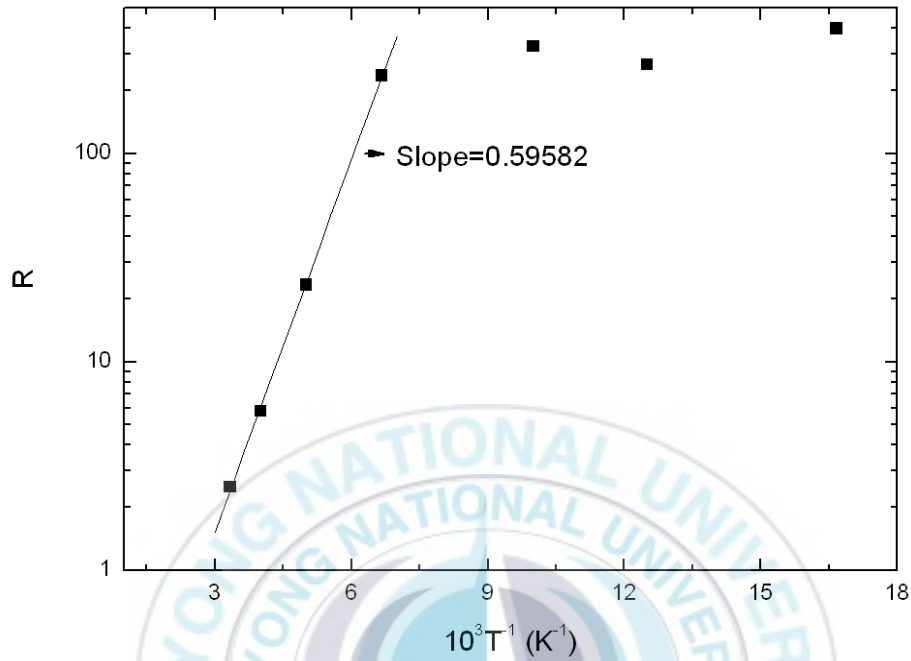$$\Delta E = 0.59582 \times (10^3 \times \ln 10) \times 1.38 \times 10^{-23} = 0.118 \, eV = 950 \, cm^{-1}$$

Fig. 4.10. R is the ratio of the integrated intensity between the line emission and the band emission as a function of 10^3T^{-1} for the LiBaF$_3$: Eu^{2+} single crystal.

The value of the ΔE reported by Sommerdijk et al. [3] is 800 cm^{-1}. However, we think our value (950 cm^{-1}) is better than that one. Using the helium gas bath equipment, we could measure the date of LiBaF$_3$:Eu^{2+} single crystals from 15 K to 300 K. After measuring the emission spectra and calculating the activation energy between the excited *4f* and *5d* level, we can draw a configurational coordinate diagram of the LiBaF$_3$:Eu^{2+} single crystal which is shown in figure 4.11.
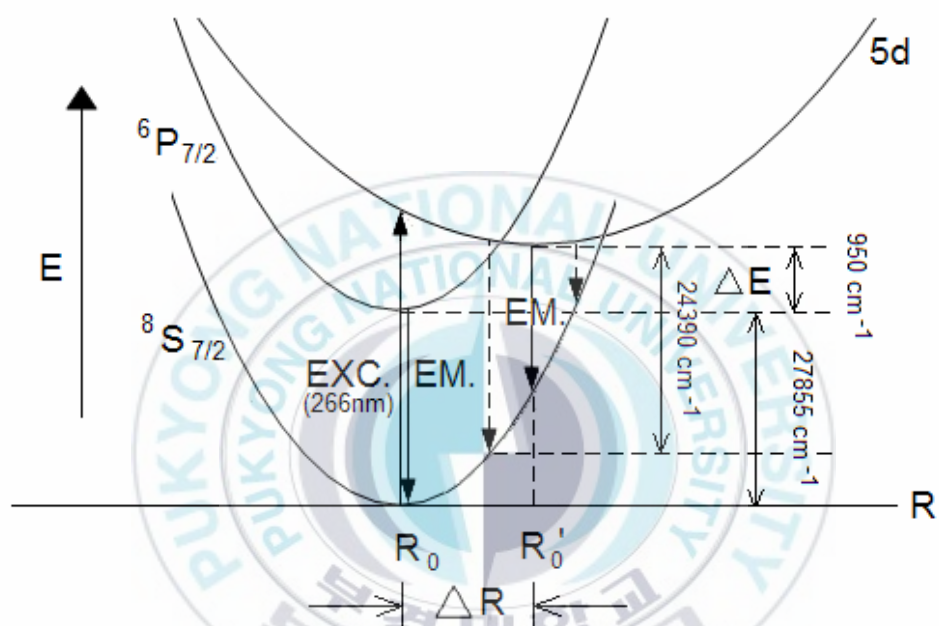
Fig. 4.11 The configurational coordinate model for the LiBaF$_3$:Eu^{2+} single crystal. EXC. is the excitation process. Em. is the emission process. ΔE is the energy difference between the excited *4f* and *5d* levels.

4.4.3 The nonradiative transition rate in the LiBaF$_3$:Eu^{2+} (2 mol%) single crystal

As shown in the figure 4.5 and 4.9, the interaction between the excited *4f* and *5d* levels occurs by the direct-phonon process. But the mechanism has not yet been reported in detail. The nonradiative transition rate is also unknown. The nonradiative rate from the *5d* to *4f'* level is called W_{df} and from the *4f'* to *5d* is W_{fd}. The radiative rate from the *5d* to the ground state is named W_d and from the *4f'* to the ground state is W_f. All the expressions are the same with those in the Chap. 2. The lifetime of the *4f'* is τ_f and *5d* is τ_d.
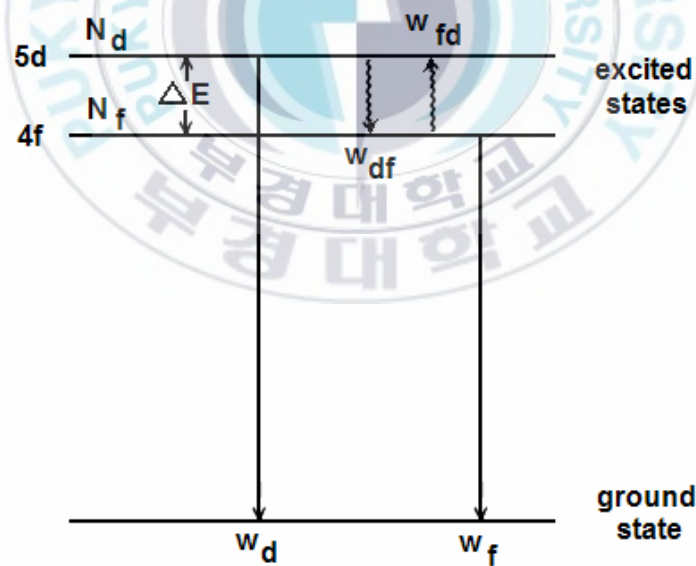

Fig. 4.12. Energy level scheme of the excited *4f* and *5d* transitions. Wavy arrows and straight arrows indicate the nonradiative and radiative transitions, respectively.

Dang et al. [22] and Tsuboi et al. [23] have discussed kinetic models in different crystals which also have the interaction between two excited states. Our model is shown in the figure 4.12. In this figure, the energy gap (ΔE) of the excited *4f* and *5d* level has been calculated in the former section. The ratio of the degeneracies g_d/g_f of the two excited levels is called *g*. Using the approximation $g_d = g_f$ [3], the value is *g* =1. The nonradiative transition from the *5d* to *4f'* levels occurs with a probability W_{df}, while the reverse process has a probability as

$$W_{fd} = W_{df} \exp(-\Delta E / kT) \qquad \text{(4-4-1)}$$

The rate equations for the populations N_d and N_f in the *5d* and *4f'* levels are given as follows [22], respectively,

$$\frac{dN_d}{dt} = -(W_{df} + W_d)N_d + gW_{fd}N_f \qquad \text{(4-4-2)}$$

$$\frac{dN_f}{dt} = -(gW_{fd} + W_f)N_f + W_{df}N_d \qquad \text{(4-4-3)}$$

Equation (4-4-2) and (4-4-3) lead to a quadratic equation for lifetime *t*:

$$[gW_{fd}W_d + W_f(W_{df} + W_f)]\tau^2 - (W_{df} + gW_{fd} + W_f + W_d)\tau + 1 = 0$$

$$\text{(4-4-4)}$$

The two solutions of this equation we considered give two constants of lifetime: a fast component τ_d and a slow component τ_f.

We assume for the moment that the relaxation process between the *4f'* and *5d* levels is one-phonon process, so that $W_{fd} = Cn$, where *C* is a parameter and *n* is the Bose-Einstein distribution function,

$$n = [\exp(\Delta E / kT - 1]^{-1} \tag{4-4-5}$$

From the equation (4-4-1) and (4-4-5), we know that $W_{df} = C(n+1)$

The parameters W_{fd} and W_{df} are functions of the variable *n* and *C*. Variable *n* is the function of the constant ΔE. Finally, there remain four parameters: *C*, W_d, W_f and ΔE. ΔE has been calculated in the Section 4.4.2, and its value is 950 cm^{-1}. The parameters W_d and W_f can be determined from the best fitting to the experimental data: τ_d (T) and τ_f (T) at 0 K, respectively. The τ_d (T) can be considered as the value of the short component lifetime of the *5d* level at 410 nm in low temperature shown in figure 4.13 (a).The τ_f (T) can be considered as the value of the temperature dependent lifetime of the excited *4f* level at 359 nm shown in figure 4.13 (b).
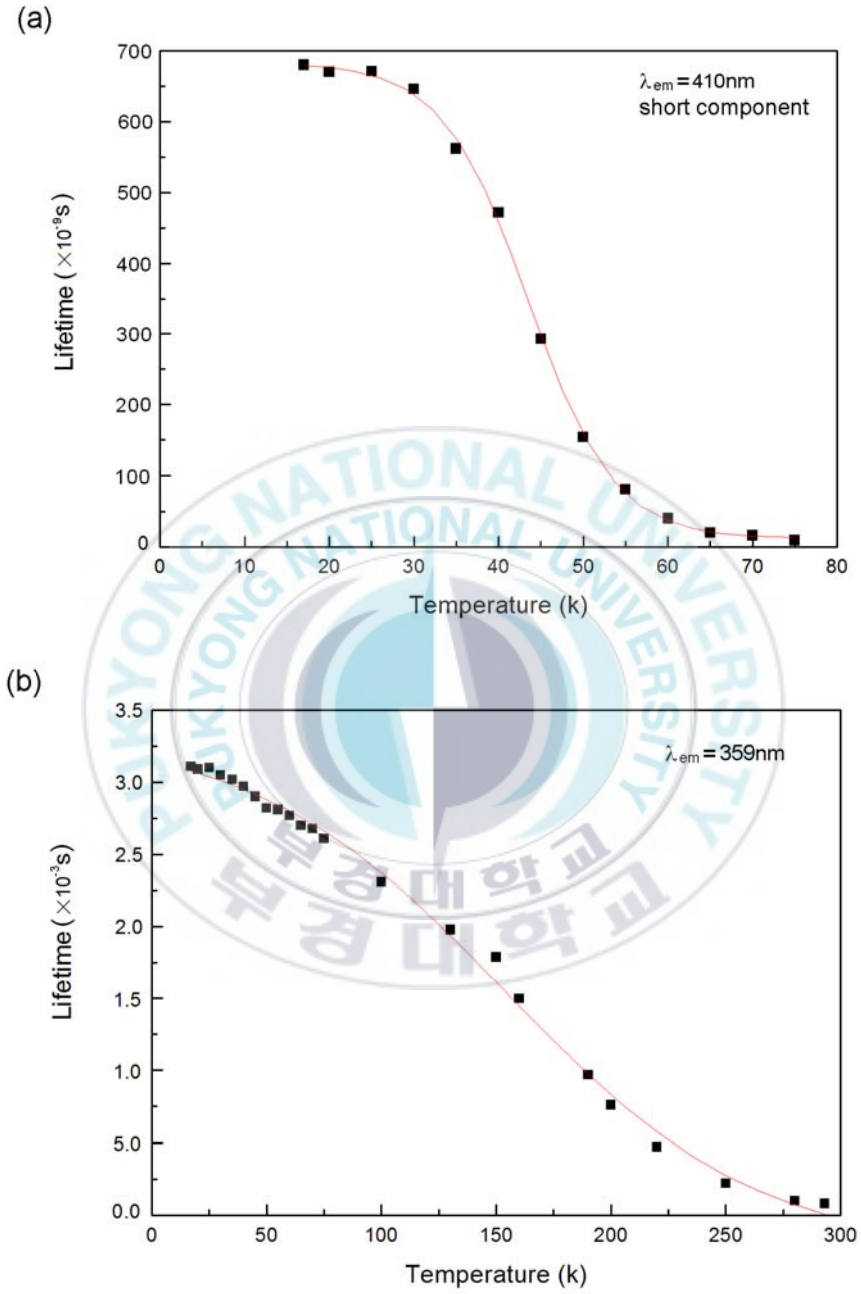
Fig. 4.13 Best fitting for the experimental data of the $\tau_d(T)$ (a) and $\tau_f(T)$ (b). The points in these two figures are experimental data and two lines are fitting data. The values of τ_f and τ_d at 0 K are 3.14×10^{-3} s and 6.827×10^{-7} s, respectively.

Best fitting for the experimental date of the τ_f(T) and τ_d(T) has been done to get the value of the τ_f and τ_d at 0 K, and W_f = 1/τ_f(0 K), W_d = 1/τ_d(0 K). From the fitting curves, W_f and W_d are estimated to be 318 s^{-1} and 1.465×10^6 s^{-1}, respectively. Thus, the equation (4-4-4) can be written as,

$$C = \frac{-W_f W_d \tau^2 + (W_f + W_d)\tau - 1}{[(W_f + W_d)n + W_f]\tau^2 - (2n+1)\tau}$$

(4-4-6)

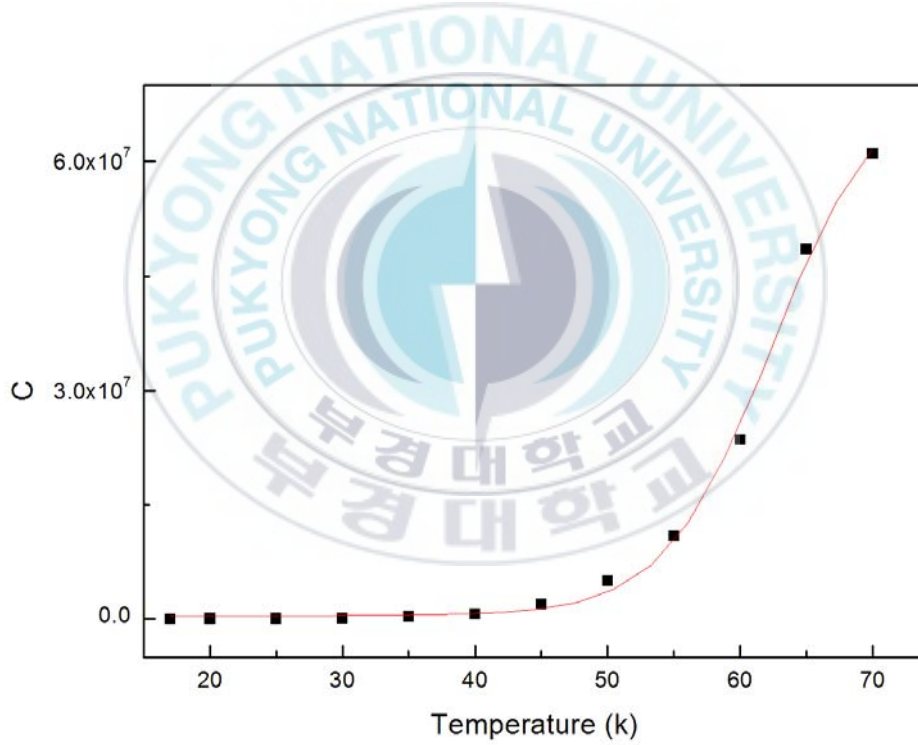Fig.4.14 The fitting curve of temperature dependent parameter C(T) at low temperature. At 0 K, the value of it is 4.331×10^5 s^{-1}. The points in this figure are experimental data and the line is fitting data.

53

The temperature dependent data of τ_d(T) is used as one solution of the equation (4-4-5). Then, a fitting curve of temperature dependent C(T) can be drawn at low temperature in figure 4.14 and the value of parameter C at 0 K is 2.309×10^{-6} s, viz. 4.331×10^{5} s^{-1}.

The temperature dependent curve of the variable n is shown in the figure 4.15, which indicates that the value of n is nearly zero at low temperature. Thus, $W_{fd}=C\,n \approx 0$ and $W_{df}= C\,(n+1) = C = 4.331\times10^{5}$ s^{-1}, at 0 K. The values of all parameters at 0 K are listed in table 4.1.
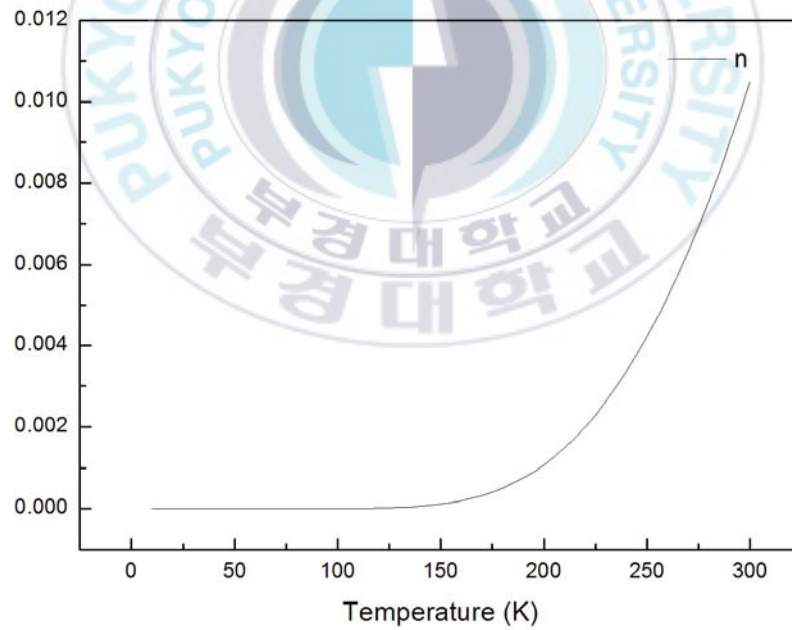

Fig. 4.15 The temperature dependent curve of the variable n is calculated from the equation 4.4.5.

Table 4.1 The values of all parameters at 0 K.

W_f	318 s^{-1}
W_d	1.465×10^6 s^{-1}
W_{fd}	≈ 0
W_{df}	4.331×10^5 s^{-1}
n	≈ 0
C	4.331×10^5 s^{-1}

The time-resolved (500 μs) emission spectra of the LiBaF$_3$:Eu^{2+} (2 mol%) single crystal from 20 K to 300 K were measured and shown in the figure 4.16. The intensity ratio of the *4f'-4f* and *5d-4f* emission depends strongly on the temperature. At low temperature, the intensity of the *4f'-4f* emission is so strong that the *5d-4f* broad band emission is hard to be observed at a long time-delay (500 μs). The intensity ratio of them approaches infinity when the temperature is lower than 150 K. Although the intensity is so weak that it nearly disappears, a very weak emission spectrum could be found at around 410 nm at 20 K. Consider the decays of the *4f'* and *5d* long component emissions shown in figure 4.9, two entire decay curves from 13 K to 300 K shown in figure 4.17 and the ratio of W_{fd} / W_{df} shown in figure 4.18, we can conclude that

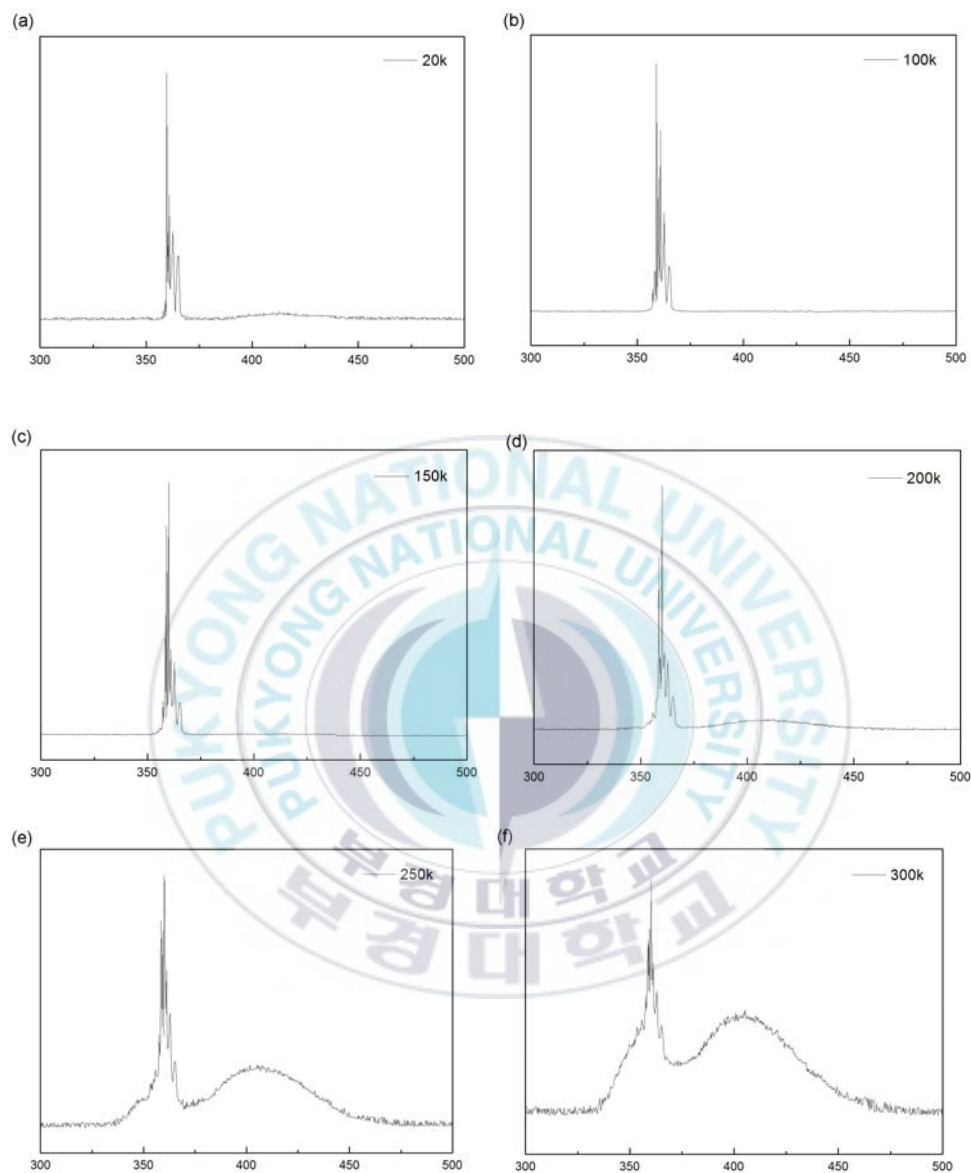Fig. 4.16 Time-resolved (500 µs) emission spectra of the LiBaF$_3$:Eu^{2+} (2 mol%) single crystal from 20 K to 300 K excited by 266 nm laser. At high temperature, the intensity of the broad band emission is much stronger than that in low temperature.
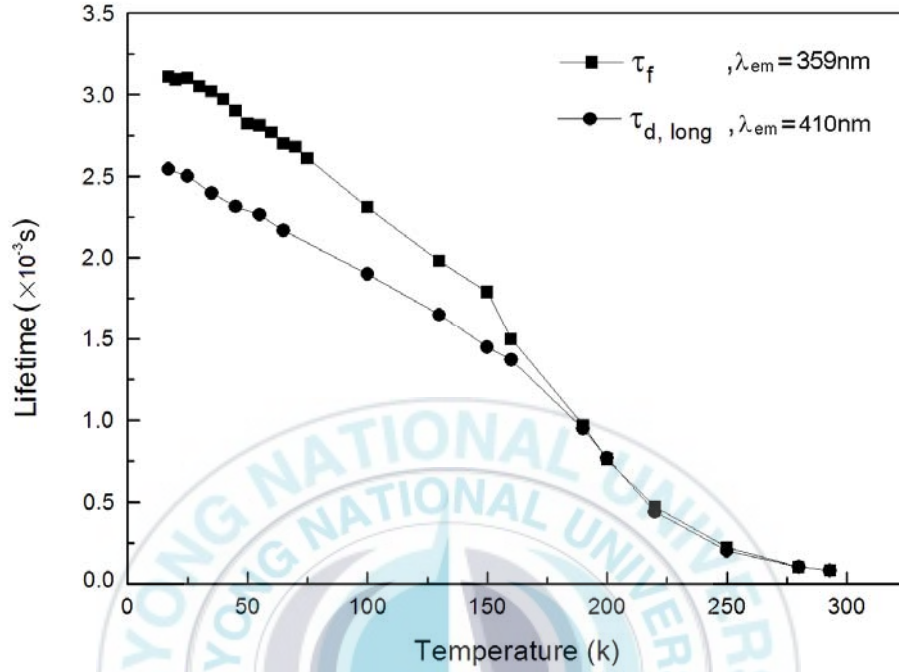
56

Fig.4.17 The entire decay curves of the LiBaF$_3$:Eu^{2+} (2 mol%) single crystal from 13 K to 300 K. τ_f is the lifetime of the *4f'-4f* emission at 359 nm, and $\tau_{d, long}$ is the lifetime of the *5d-4f* long component emission at 410 nm.

(1). T < 75 K. W_{fd} / W_{df} ≈ 0. In comparison with the nonradiative transition rate from the *4f'* to *5d* level (W_{fd}), the rate from the *5d* to *4f'* level (W_{df}) nearly approaches infinity, which indicates that most of the nonradiative transitions occur from the *5d* level to the *4f'* level and few nonradiative transitions are from the *4f'* to *5d* level. This is the reason why the time-resolved (500 µs) spectra of the *5d* long component emission could not be observed in very low temperature. However, at 20 K, the decay of the *5d* short component is 660 ns and the thermal-quenching effect is very low,

57

thus, a very weak spectrum at around 410 nm can be seen.

(2). 75 K < T < 150 K. In this range of temperature, the ratio of W_{fd}/W_{df} is also very small. But from the figure 4.18, we can find this value increases gradually. The nonradiative transition rate from the $4f'$ to $5d$ level increases with temperature. Although the intensity of the $5d$-$4f$ emission spectra at around 410 nm is also very weak, the intensity of the $4f'$-$4f$ emission at 359 nm decreases. In comparison with the $4f'$-$4f$ transition, the $5d$-$4f$ transition is parity allowed transition. Thus, the influence of temperature effect on the $5d$-$4f$ transition is much lower than that of $4f'$-$4f$ transition. As a result, the decreasing lifetime of the $5d$ long component emission is smaller than that of the excited $4f$ emission.

(3). T > 150 K. The ratio of W_{fd}/W_{df} increases to an understandable level. Also, the value increases gradually, but the increasing rate is lower than that at low temperature. The absolute value of W_{fd} is very large compared to it at low temperature. Above 150 K, the lifetimes of the $4f'$ and $5d$ level are nearly the same, which indicates that most of the excited ions at $5d$ level come from $4f'$ level and the transitions from $5d$ state to ground state also come from the $4f'$ state. The intensity of the line emission peak at 359 nm is just two times as the broad emission band at around 410 nm when the temperature is 300 K.
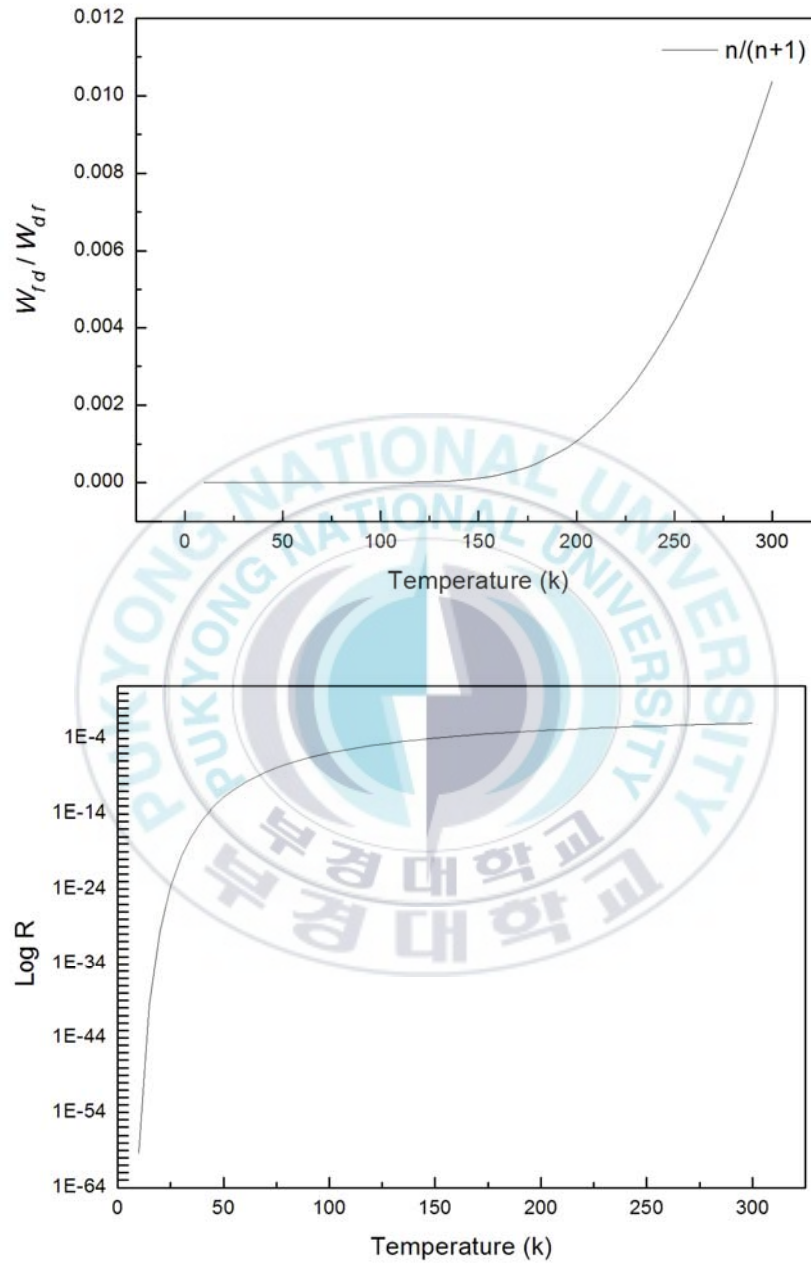
Fig. 4.18 The ratio (W_{fd}/W_{df}) of the nonradiative transition rates from 10 K to 300 K. $W_{fd}/W_{df} = Cn / [C(n+1)] = n/(n+1)$. Log R is the logarithmic value of the ratio.

5. Conclusion

The Eu-doped $LiBaF_3$ single crystals were prepared by the Czochralski method. The $LiBaF_3$ melted incongruently and the single crystal grew from a non-stoichiometric melt to avoid other phase precipitations. The different mole ratios of the LiF and BaF_2 powder influence the purity of the $LiBaF_3$ compounds greatly. The best mole ratio is 3:2. Also, the effect of two times calcinations can enhance the purity of the compounds. Having many times of experiment, we find that the initial temperature cooling rate should be lower than 1 ℃/h and a good initial part of the crystal is very important which requires the neck of the crystal should be long and small. Since the crucible is big without a platinum attemperator and the $LiBaF_3$ single crystal is grown from the non-stoichiometric melt, the pulling speed should be lower than 1 mm/h. Otherwise, there would be many cracks inside the crystal. Different rotation speeds yield the different temperature fields which also influence the optical properties of the $LiBaF_3$ single crystal.

The emission spectra of the *4f'-4f* transition at 359 nm and the *5d-4f* transition at around 410 nm are observed. The energy level of the excited *4f* state is lower than the *4f5d* state. The intensity of emission spectra increased with the concentration of Eu^{2+} ions doped below 2 mol%. Because the *4f'-4f* transition is parity forbidden and the *5d-4f* is parity allowed, the figures of the spectrum are sharp line and broad band, respectively. The

zero-phonon line of the *4f'-4f* transition is observed with some Stokes and anti-Stokes vibrational lines.

The temperature dependent decay curves show an unusual energy transition process in the $LiBaF_3:Eu^{2+}$ (2 mol%) single crystal. The nonradiative transitions between the excited *4f* and *5d* states are observed. The emission of the *4f'-4f* transition "borrows" from the *5d-4f* transition. Apparently, it has a probability to "return" to the *5d-4f* transition. By using the temperature dependent lifetimes of Eu^{2+} ion, the activation energy (ΔE) between the excited *4f* and lowest *5d* state can be calculated and the value is 950 cm^{-1} (0.118 eV). A best fitting method is used to obtain the radiative rate of the *4f'-4f* and *5d-4f* transitions. The fitting curves show W_f = 318 s^{-1} and W_d = 1.465×10^6 s^{-1}. In comparison with the time-resolved emission spectra and the lifetimes of the *4f'* and *5d* states, the mechanism of this unusual transition could be illustrated. At lower temperature, the transition rate from the *5d* to *4f'* state is much stronger than that from the *4f'* to *5d* state. With increasing of the temperature, the ratio of W_{fd}/W_{df} is bigger than that at lower temperature. Thus, the intensity of long component emission at 410 nm increases gradually. Above the 150 K, the short component emission of the $LiBaF_3:Eu^{2+}$ (2 mol%) at 410 nm nearly disappears.

References

1. J. Rubio O., Journal of Physics and Chemistry of Solids, **52**, 101 (1991).

2. G. Blasse and B. C. Gramaier, "Luminescent Materials", Springer (1994).

3. J. L. Sommerdijk, J. M. P. J. Verstegen and A. Bril, Journal of Luminescence, **10**, 411 (1975).

4. R. Alcala, D. K. Sardar and W. A. Sibley, Journal of Luminescence, **27**, 273 (1982).

5. S. L. Baldochi and J. Y. Gesland, Materials Research Bulletin, **27**, 891 (1992).

6. M. Marsman, J. Andriessen and C. W. E van Eijk, Physical Review B, **61**, 16477 (2000).

7. Y. Tan and C. Shi, Journal of Physics and Chemistry of Solids, **60**, 1805 (1999).

8. R. Leckebusch, A. Neuhaus and K. Recker, Journal of Crystal Growth, **16**, 10 (1972).

9. S. L. Baldochi, V. L. Mazzocchi, C. B. R. Parente and S. P. Morato, Materials Research Bulletin, **29**, 1321 (1994).

10. A. Bensalah, K. Shimamura, T. Fujita, H. Sato, M. Nikl and T. Fukuda, Journal of Alloys and Compounds, **348**, 258 (2003).

11. S. N. Achary, A. K. Tyagi, T. K. Seshagiri and V. Natarajan, Materials Science and Engineering B, **129**, 256 (2006).

12. A. V. Gektin, N. V. Shiran and V. V. Voronora, IEEE Transactions on Nuclear Science, **44**, 857 (1997).

13. A. Meijerink and G. J. Dirksen, Journal of Luminescence, **63**, 189 (1995).

14. S. Fujihara, Y. Kishiki and T. Kimura, Journal of Solid State Chemistry, **177,** 1032 (2004).

15. R. N. Hua, Z. H. Jia, D. M. Xie and C. S. Shi, Chinese Chemical Letters **13**, 1021 (2002).

16. N. Shiran and V. Voronova, Journal of Luminescence, **87-89**, 561 (2000).

17. C. T. Xia and C. S. Shi, Materials Research Bulletin, **32**, 107 (1997).

18. M. Henke, J. Perbon and S. Kuck, Journal of Luminescence, **87-89**, 1049 (2000).

19. A.V. Gektin, Journal of Luminescence, **87-89**, 1283 (2000).

20. A. Meijerink, Journal of Luminescence, **55**, 125 (1993).

21. E. S. Kim, "Luminescence Properties of Er^{3+} ions doped in calcium Niobium Gallium Garnet Crystal", thesis for the degree of master, Pukyong National University (2008).

22. D. L. S. Dang, R. Romestain, and D. Simkin, Physical Review B, **18**, 2989 (1978).

23. T. Tsuboi and P. Silfsten, Journal of Physics: Condensed Matter, **3**, 9163 (1991).

Acknowledgements

The accomplishment of this paper benefits from the enlightenment of my supervisor, Professor Hyojin Seo, whose inspiring insights, generous encouragements, and enthusiastic instructions have facilitated me much throughout my thesis writing. His penetrating and insightful comments afford me with inspiring source. He has been in constant concern about my paper, spared no pains to entertain my thesis draft. I would also like to extend my sincere thanks to Professor Byungkee Moon and Byeongeog Jun. Thanks to their instructive guidance and comprehensive education during the two years' schooling.

I would like to express my heartfelt gratitude to Prof. Yanlin Huang and Dr. Zuolin Fu. Without their consistent and illuminating instruction, this thesis could not have reached its present form.

I am also greatly indebted to Dr. KyoungHyuk Jang, HyunKyoung Yang, and EunSik Kim who gave me their help and time in listening to me and helping me work out my problems during the difficult course of the thesis.

Finally, my great gratitude also goes to those writers whose works I have perused and benefited greatly from without which the completion of the thesis would not have been possible.